Porous oligomeric materials synthesised using a new, highly active precatalyst based on ruthenium(iii) and 2-phenylpyridine

Kacper Poblocki, Katarzyna Jarzembska, Radoslaw Kamiński, Joanna Drzeżdżon, Krystyna Deresz, Dominik Schaniel, Anna Gołąbiewska, Barbara Gawdzik, Przemyslaw Rybiński, Dagmara Jacewicz

Porous oligomeric materials synthesised using a new, highly active precatalyst based on ruthenium(III) and 2-phenylpyridine

Kacper Pobłocki, *[a] Katarzyna N. Jarzembska,[b] Radosław Kamiński,[b] Joanna Drzeżdżon,[a] Krystyna A. Deresz,[b] Dominik Schaniel,[c] Anna Gołąbiewska,[a] Barbara Gawdzik,[d] Przemysław Rybiński[d] and Dagmara Jacewicz *[a]

[a]Department of Environmental Technology, Faculty of Chemistry, University of Gdansk, Wita Stwosza 63, 80-308 Gdansk, Poland.
E-mail: kacper.poblocki@phdstud.ug.edu.pl, dagmara.jacewicz@ug.edu.pl
[b]Department of Chemistry, University of Warsaw, Żwirki i Wigury 101, 02-089 Warsaw, Poland
[c]Université de Lorraine, CNRS, CRM2, F-54000 Nancy, France
[d]Institute of Chemistry, Jan Kochanowski University, Uniwersytecka 7, 25-406 Kielce, Poland

There are few literature reports on using precatalysts based on ruthenium(II/III) ions in the polymerization of olefins. Therefore, a new coordination compound was designed based on ruthenium(III) ion and 2-phenylpyridine. The resulting monocrystal was characterized by X-ray diffraction (XRD), solid-state (photo)IR spectroscopy, scanning electron microscopy (SEM), and thermogravimetric analysis (TGA). The new ruthenium(III) complex compound was used as a precatalyst in the oligomerization reactions of ethylene, 2-propen-1-ol, 2-chloro-2-propen-1-ol, 3-butene-2-ol and 2,3-dibromo-2-propen-1-ol with methylaluminoxane and ethylaluminium dichloride as activators. The catalytic activity of the newly discovered ruthenium(III) complex compound ranges from 159.5 (for 2-chloro-2-propen-1-ol) to 755.6 (for ethylene) g $mmol^{-1}$ h^{-1} bar^{-1}, indicating that it is a chemical compound with high catalytic activity. In addition, the oligomerization reaction products were subjected to physicochemical characterization, using BET (Brunauer–Emmett–Teller isotherm), mass spectrometry (MALDI-TOF-MS), Fourier transform infrared (FT-IR) spectroscopy, NMR, TGA, differential scanning calorimetry (DSC), and the morphology of the porous polymeric materials was investigated by SEM. The distinguishing feature of the obtained precatalyst is its high catalytic activity under mild reaction conditions, a rare phenomenon. Compared with other precatalysts, it is the most active ruthenium(II/III) ion-based catalytic material used in oligo- and polymerization reactions of ethylene.

Introduction

Precatalysts based on transition-metal ions are still intensively designed thanks to their wide applications in the coordination polymerization of olefins.[1] Continuous development has led to an increase in the global demand for high-value petrochemical intermediates, alpha- and beta-olefin polymer materials, e.g., high-density polyethylene (HDPE), isotactic polypropylene (iPP), cis- and trans-polydienes, and ethylene–propylene elastomers (EPE).[2–4] Large-scale polyolefins are mainly produced by free-radical polymerization, or with the use of Ziegler–Natta catalysts. Their high production volume is an incentive to further improve the efficiency of alkene polymerization reactions and the design of catalytic systems with very high catalytic activity (above 1000 g $mmol^{-1}$ h^{-1}).[4,5] The basis for achieving this goal is a "well-defined precatalyst", i.e., chemical entities that we can crystallize from a solution and determine the structure, including the oxidation state of the metal ion and the coordination sphere (geometry).[6–8] This type of welldefined catalyst is sufficiently stable, which allows the spectroscopic and X-ray characterization of its structure, as well as the observation and control of the formation of intermediate products and the proposing of the reaction's mechanism.[7,8]

However, the high catalytic activity of organometallic compounds, the long duration of the process, and the performance of the reaction under reduced pressure and at elevated temperature lead to a dramatic increase in the cost of the polymerization process. Therefore, scientific research is focused on designing new, stable post-metallocene precatalysts that can be used in olefin polymerization reactions under mild reaction conditions (Fig. 1).[9–12]

Ruthenium-based catalysts are mostly used in olefin metathesis, e.g., Grubbs catalysts.[13] To date, few scientific publications relate to ruthenium precatalysts used in olefin polymerization.[14] A flagship example is the research of the Nomura group,[15] which synthesized ruthenium(II) complexes with a [2,6-bis[(4S)-4-isopropyl-2-oxazolin-2- yl]pyridine] (pybox) ligand, namely [RuX_2(pybox)(ethylene)] (where X = Cl or I). Scientists developed a catalytic system based on a complex compound of ruthenium(II) and methylaluminoxane (MAO) and applied it in the homopolymerization of ethylene.[15] The catalytic activity of the ruthenium complex compound was 0.28–2.14 kg polyethylene mol^{-1} h^{-1}. However, in the ethylene/1-hexene copolymerization process, the catalytic activity [RuX_2(pybox)(ethylene)] was 1.34–1.72 kg of polymer mol^{-1} h^{-1}.[15] A very similar compound Ru-diiminopyridine designed by the Dias, Brookhart, and White group[16] turned out to be completely inactive, although the analogous Fe(II)-diiminopyridine complex showed excellent activity towards the insertional polymerization of ethylene.[16] In turn, Simal et al.[17] reported the compound [$RuCl_2$(p-cymene)(PCy_3)] (p-cymene = 4-isopropyltoluene; PCy = cyclohexylphosphane), which they used as a catalyst in the controlled radical polymerization of vinyl monomers without the use of an activator. Methyl methacrylate was polymerized in 100% yield, while styrene, n-butyl acrylate,
isobornyl methacrylate and tert-butyl methacrylate were polymerized in 64–80% yield. [$RuCl_2$(p-cymene)(PCy_3)] did not catalyze the vinyl acetate polymerization reaction.[17] From the above, it can be concluded that there is a large
research niche in the design and synthesis of highly active ruthenium(II/III/IV) precatalysts.[18–20] On the other hand, if there are complex compounds based on ruthenium ions, they show low (1–10 g $mmol^{-1}$ h^{-1} bar^{-1}) or moderate catalytic activity (10–100 g $mmol^{-1}$ h^{-1} bar^{-1}).[4,5] Therefore, we proceeded to design the synthesis of a new catalytic complex, using ruthenium(III) salt and 2-phenylpyridine as a ligand. This is becausethe recently synthesized oxovanadium(IV) microclusters with 2-phenylpyridine showed very high catalytic activity in the oligomerization of allyl alcohol, 3-buten-2-ol, and 2,3-dibromo-2-propene-1-ol.[8] The aim of our work was to fill the research niche by the design, synthesis, and physicochemical characterization of a new potential ruthenium(III) precatalyst. In-depth structural studies were made

possible by growing single crystals of the [Ru(2-phenylpyridine)(Cl)$_2$(DMSO)(NO)] compound (hereafter Ru1). In addition, we checked the catalytic properties of the Ru(III) coordination compound in the process of olefin oligomerization (Fig. 1) and physicochemically characterized the obtained oligomers. Since coordination polymerization probably takes place, we expect linear structures of oligomers (Fig. S34–S38).

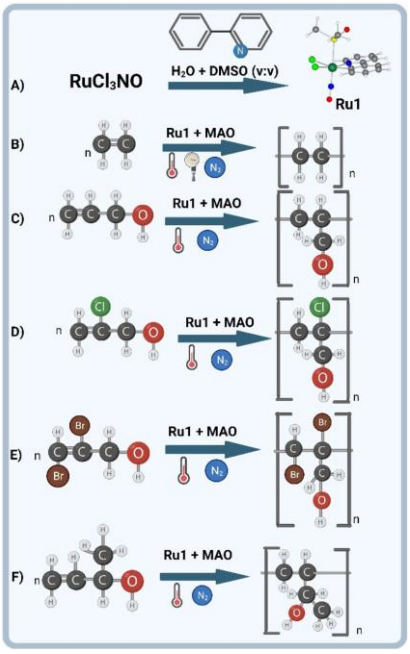

Fig. 1 Scheme of the Ru1 synthesis (A). Scheme of (B) ethylene, (C) allyl alcohol, (D) 2-chloro-2-propen-1-ol, (E) 2,3-dibromo-2-propen-1-ol, and (F) 3-buten-2-ol oligomerizations. Created with BioRender.com.

Results and discussion

A new complex compound based on ruthenium(III) ion and 2-phenylpyridine was synthesized and structurally characterized (Fig. S33). The physicochemical and catalytic properties of [Ru(2-phenylpyridine)(Cl)$_2$(DMSO)(NO)] (hereafter referred to as Ru1) are described in this report.

Crystal structure

The structure of Ru1 was investigated with the single-crystal XRD method. Ru1 crystallizes in the triclinic P-1 space group with one molecule in the asymmetric part of the unit cell (Fig. 2). The metal coordination sphere adopts an approximately octahedral geometry. The Ru(III) center forms a C–Ru bond with the phenylpyridine fragment and is further coordinated by the nitrogen atom of the same ligand. The metal atom is also coordinated by chloride anions, which altogether result in the quasi-square base of the bipyramid. Above and below this molecular plane, two ambidentate ligands are attached, i.e., NO and DMSO. The NO group adopts an (η^1-NO)-nitrosyl binding mode, while the DMSO moiety is O-bound to the ruthenium center. Selected X-ray data are summarized in Table 1.

Molecules in the crystal structure of Ru1 are arranged in such a way that the DMSO moieties of the adjacent molecular layers, parallel to the (010) crystal plane, are directed towards one another (ESI). The same applies to the NO ligands. The crystal structure is stabilized by numerous hydrogen-bond-like contacts formed by the O1 oxygen atom or chloride ligands with the aromatic hydrogen atoms or with the methyl group. Additionally, π-stacking interactions between the neighbouring phenylpyridine moieties should be noted, as well as the weak C–H···π contacts between the aromatic rings and methyl fragments. All key interactions are well visualized with the aid of Hirshfeld surfaces[21–23] in Fig. S1 and S2 in the ESI, whereas the selected dimeric motifs are presented in Fig. 3. The interaction energies characterizing each of these structural motifs are presented in Table 2. The ambidentate ligands, NO and DMSO, are engaged in hydrogen bonds and C–H···π interactions. The NO group interacts with hydrogen atoms from the phenyl ring forming two motifs – D2 and D6. The interaction energy between the components of the D2 dimer is relatively weak (−11.35 kJ mol^{-1}), which favors potential isomerization reaction. In turn, the D6 dimer is held by two types of interactions, a weak hydrogen bond-like contact between the NO oxygen atom and the H13 aromatic hydrogen atom, and a π-stacking interaction. The overall interaction energy calculated for this motif is thus more advantageous (−63.89 kJ mol^{-1}). Motifs stabilized by interactions involving the DMSO group, i.e., D4 and D5, are characterized by the most significant interaction energy values, i.e. −84.62 kJ mol^{-1} and −124.14 kJ mol^{-1}, respectively.

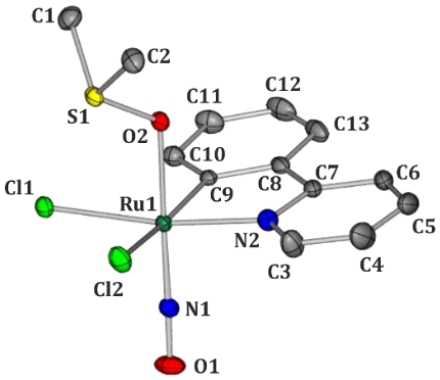

Fig. 2 Molecular structure of the Ru1 complex derived from the X-ray diffraction data. Atomic thermal motion is represented as ellipsoids (50% probability level), and hydrogen atoms are omitted for clarity.

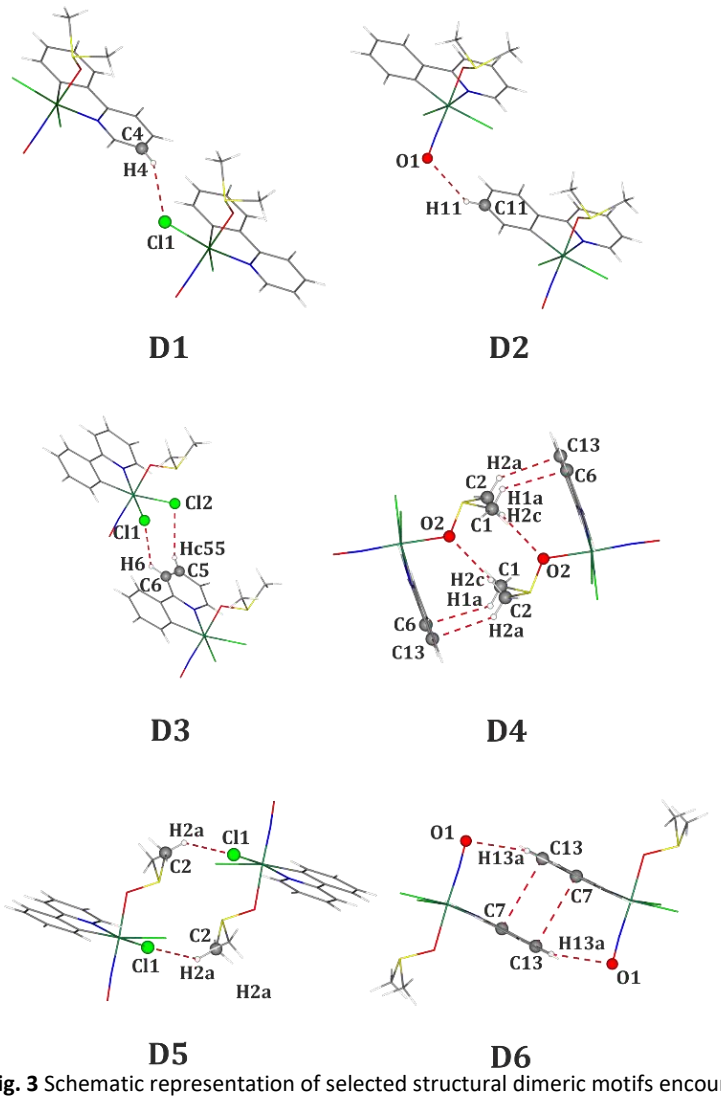

Fig. 3 Schematic representation of selected structural dimeric motifs encountered in the Ru1 crystal structure.

Table 1. Selected crystal structure and refinement parameters.

Moiety formula	$C_{13}H_{14}O_2N_2RuCl_2S$
Moiety formula mass, M_r / a.u.	434.34
Crystal system	triclinic
Space group	$P\bar{1}$ (No. 2)
Z	2
F_{000}	432
Crystal colour & shape	red triangular block
Crystal size / mm^3	0.06 × 0.12 × 0.12
T / K	100
a / Å	8.616(2)
b / Å	8.795(2)
c / Å	11.944(2)
α / °	97.23(3)
β / °	95.61(3)
γ / °	114.26(3)
V / Å^3	807.4(4)
d_{calc} / g·cm^{-3}	1.787
θ range	2.58−37.47°
Absorption coefficient, μ / mm^{-1}	1.434
No. of reflections collected / unique	32046 / 8197
R_{int}	2.58%
No. of reflections with $I > 3\sigma(I)$	7363
No. of parameters / constraints	190 / 56
$R[F]$ (all data)	2.78%
$wR[F^2]$ (all data)	5.99%
$\varrho_{res}^{min/max}$ / e·Å^{-3}	−0.64 / +0.67

Table 2. Selected dimeric motifs present in the **Ru1** crystal structure: geometrical parameters and interaction energy values (E_{int}; DFT(B3LYP)/LANL2DZ level of theory with the Grimme dispersion correction applied; geometries with the X−H neutron-normalized distances were used for computations).

Motif	E_{int} / kJ·mol^{-1}	*Selected interactions*	$d_{H\cdots A}$ / Å	$d_{D\cdots A}$ / Å	$\theta_{D-H\cdots A}$ /°
D1[#1]	−15.70	C4−H4···Cl1	2.81	3.658(3)	147.86
D2[#2]	−11.35	C11−H11···O1	2.70	3.470(3)	137.34
D3[#3]	−32.57	C5−H5···Cl2	2.94	3.590(3)	126.31
		C6−H6···Cl1	2.94	3.643(2)	131.38
D4[#4]	−84.62	C1−H1a···C6(π)	2.90	3.550(2)	126.18
		C2−H2a···C13(π)	2.86	3.577(2)	132.73
		C2−H2c···O2	2.55	3.505(3)	171.68
D5[#5]	−124.14	C2−H2a···Cl1	2.85	3.600(2)	135.43
D6[#6]	−63.89	C13−H13…O1	2.72	3.562(3)	146.74
		C7(π)···C13(π)		3.526(2)	

Symmetry operations: (#1) *x*−1, *y*−1, *z* (#2) *x*, *y*−1, *z*, (#3) *x*−1, *y*, *z*, (#4) −*x*+1, −*y*+1, −*z*+1, (#5) −*x*+2, −*y*+1, −*z*+1, (#6) −*x*+1, −*y*+1, −*z*+2.

In the centrosymmetric dimer D4, both hydrogen bond-like contacts and dispersive interactions are encountered. Indeed, the oxygen atom from DMSO forms a hydrogen bond-like interaction with the hydrogen atom from the DMSO ligand of the adjacent molecule. Additionally, hydrogen atoms from the methyl groups of DMSO are involved in the edge-to-face interaction. The centrosymmetric D5 motif is described by the most favorable interaction energy between its components among all the analyzed dimers thanks to the significant electrostatic contribution. It is stabilized by a pair of strong interactions between a hydrogen atom from the methyl group of DMSO and the chlorine ligand. In view of the above, DMSO is better stabilized in the crystal structure than NO. Consequently, the latter ligand should be more mobile. In this respect, it is also worth noting the corresponding 'reaction cavity volumes' (ESI).[24] In the case of the NO group, the cavity amounts to 19.16 Å^3. This value is comparable to that calculated for the photoswitchable nitrosyl systems reported in the literature,[25,26] whereas for DMSO it is equal to 109.78 Å^3,[27] (probe radius of 1.2 Å and grid spacing of 0.1 Å). Based on several examples (ESI), there is not much of a difference in cavity sizes between the O-bound and S-bound DMSO moieties. Examples of light-induced DMSO switching have already been reported in the literature[28–32]

IR spectroscopy

Since the Ru1 molecule has two ambidentate ligands attached to the metal center, it is potentially prone to exhibiting linkage isomerism, which could be, e.g., induced by light. Here, only switching of the NO ligand is considered, as for the bulkier DMSO molecule, no solid structural and spectroscopic evidence supporting its isomerization was found. Molecular geometries of the ground state binding mode (Ru–NO) and its potential photo-induced linkage isomers (PLIs), referred to as MS1 (Ru–ON) and MS2 (side-on biding mode), were optimized at the DFT(B3LYP)/LANL2DZ level of theory (Fig. 4) and then normal-mode vibrations were computed. Based on these calculations and literature data,[27,33,34] crucial vibrational bands for the nitrosyl ligand were identified in the experimental IR spectra (Table 3, ESI), namely the ground state NO stretching vibration νNO at 1834 cm^{-1}, which decreases significantly upon light irradiation in the blue-violet spectral range, while several new vibrational bands arise, and others are shifted. The band at 1540 cm^{-1}, which is generated by blue light (405–420 nm LED light; LED – light-emitting diode), while erased with red light as well as upon heating above 150 K, is the signature of a PLI. Given its behavior, it is most probably a side-on type configuration of the NO ligand with respect to the ruthenium center (MS2). The population of this PLI is small, though. Furthermore, a light-induced NO release is observed both at room temperature and at low temperature, as evidenced by the appearance of the band around 2224 cm^{-1}.[35,36] In turn, the main feature, namely the strong band arising at 1760 cm^{-1} at low temperature, and at 1790 cm^{-1} at room temperature, corresponds to the NO stretching vibration in the PLI. It is hard to draw a conclusion about the nature of this PLI due to the other observed effects which occur in parallel. However, it can most probably be attributed to the isonitrosyl configuration of NO (MS1) but could also reflect a shift of νNO induced by the overall relaxed structure due to NO release, or due to the potential isomerization of the DMSO ligand. Additionally, so far attempts to catch the O-bound form (MS1), or the side-on isomer (MS2), via static photocrystallographic techniques have been unsuccessful. Hence, further studies are needed in order to determine the nature of photoproducts. This will be the subject of our future investigations.

Table 3. Comparison between computed normal-mode frequencies (B3LYP/LANL2DZ level of theory) and experimental values from IR spectra. All values are given in cm^{-1}.

Vibration type	*Experiment*	*Theory*		
		1_{GS}	**2_{MS1}**	**3_{MS2}**
ν_N(NO)	1834	1803	–	–
ν_O(NO)	1759 [a]	–	1720	–
ν(NO)	1540 [a]	–	–	1413
δ(Ru-N-O)	504	469	–	–

[a] After irradiation.

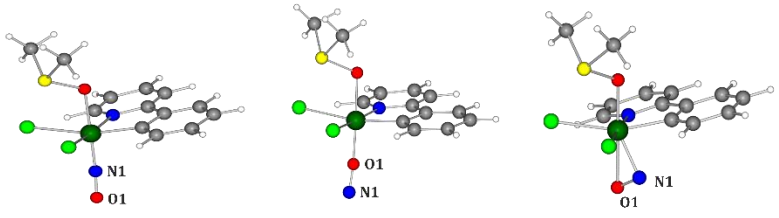

Fig. 4. Molecular structures of the Ru−(η^1-NO) ground-state (left panel) and hypothetical linkage isomers: Ru−(η^1-ON) (MS1, middle panel) and side-on Ru−(η^2-NO) (MS2, right panel).

MALDI-TOF-MS of the oligomers

Analysis of MALDI-TOF-MS spectra made it possible to identify individual mers and calculate the number of units the oligomer mixtures consist of.

The allyl alcohol oligomer mixture is composed of 7, 11, 14, 17 and 20 mers (Fig. S9). The pseudomolecular ion occurs at 410 m/z.

The oligomerization reaction of 2-chloro-2-propen-1-ol catalyzed by Ru1 produces a mixture of 4, 7, 9, 11 and 12 mers (Fig. S10). The pseudomolecular ion occurs at 411 m/z.
The oligomerization reaction of 3-buten-2-ol produced an oligomer mixture consisting of the largest number of units (six – as in the case of ethylene oligomer), i.e., 4, 5, 9, 11, 14, and 16 mers (Fig. S11). The pseudomolecular ion occurs at 334 m/z.
The oligomerization reaction of 2,3-dibromo-2-propen-1-ol catalyzed by the ruthenium(III) compound consists of a mixture of 2–5 mers (Fig. S12). Confirmation is provided by peaks at the following m/z values: 510.9; 688.9; 866.9; 1198.9.
In most spectra, peaks from the 2,5-dihydroxybenzoic acid (DHB) matrix can be distinguished at around 332.9 m/z. On the other hand, on the MALDI-TOF-MS spectrum of the ethylene oligomer mixture, no peaks originating from the matrix α-cyano-4-hydroxy acid were observed. Among the oligomerization reactions of ethylene, allyl alcohol, 2-chloro-2-propen-1-ol, 3-buten-2-ol, and 2,3-dibromo- 2-propen-1-ol, the longest chains of mers were formed in the ethylene oligomerization reaction, as the oligomer consists of a mixture of 31, 32, 33, 34, 40 and 42 mers (Fig. S13).

Thermal analysis by the TG method

An in-depth thermal analysis of the coordination complex of ruthenium(III) and oligomerization products of allyl alcohol, 2-chloro-2-propen-1-ol, 3-buten-2-ol, and 2,3-dibromo-2-propen-1-ol was determined by TGA. Ru1 undergoes a three-stage temperature decomposition. At 123 °C, the decomposition of the nitrosyl group of the ruthenium(III) complex compound probably occurs. In the second stage (T = 194 °C), the DMSO group undergoes thermolysis. The rate of the second stage of thermal decomposition is 2.53% min^{-1}, while the decomposition residue is 75.63%. The residue burns in the range of 223–388 °C. The residue after combustion is 22.25% (Fig. 5).37 A sample of the allyl alcohol oligomer undergoes a singlestage thermal decomposition in the range of 60–245 °C. The rate of thermal decay is 6.8% min^{-1}, while the residue after decomposition is 21.8%, at T = 600 °C (Fig. S14). The following chemical compounds are released: H_2O and CO, CO_2 because of the thermal decomposition of the allyl alcohol oligomer. The 2-chloro-2-propen-1-ol oligomer also undergoes singlestage thermolysis, which takes place in the range of 35–178 °C. The rate of the thermal decay stage is 7.8% min^{-1}, while the decomposition residue is 19.86% and it burns in the range of T = 600 °C (Fig. S15). Regarding the thermal decomposition of the oligomer sample obtained using Ru1 as a precatalyst, the following chemicals are released: H_2O, CO, CO_2, and HCl. By analyzing the third curve, it can be concluded that there is a single-step thermal decay of the 3-buten-2-ol oligomer, formed with the use of the Ru1 precatalyst. Thermal decomposition takes place in the range of 35–210 °C, and the rate of the thermolysis stage is 28.7% min−1 (Fig. S16). The residue after decomposition is 48.51%, and then it is burned in the range of 215–315 °C. The residue after combustion is 32.47%, while the residue at T = 600 °C is 28.76%.38 As in the three previously mentioned cases, the 2,3- dibromo-2-propen-1-ol oligomer undergoes a single-stage thermal decay in the range of 115–220 °C. The rate of thermolysis is 19.87% min^{-1}, while the residue after decomposition is 17.38%, at T = 600 °C (Fig. S17). As a result of the thermal decomposition of the 2,3-dibromo-2-propen-1-ol oligomer, the following chemical compounds are released: H_2O, CO, CO_2 and HBr. The ethylene oligomer decomposes in one step, in the range of 35–200 °C. The largest endothermic peak was recorded at 121 °C, at −91.65 µV. The rate of this stage is 10.14 mg min^{-1} (Fig. S18).

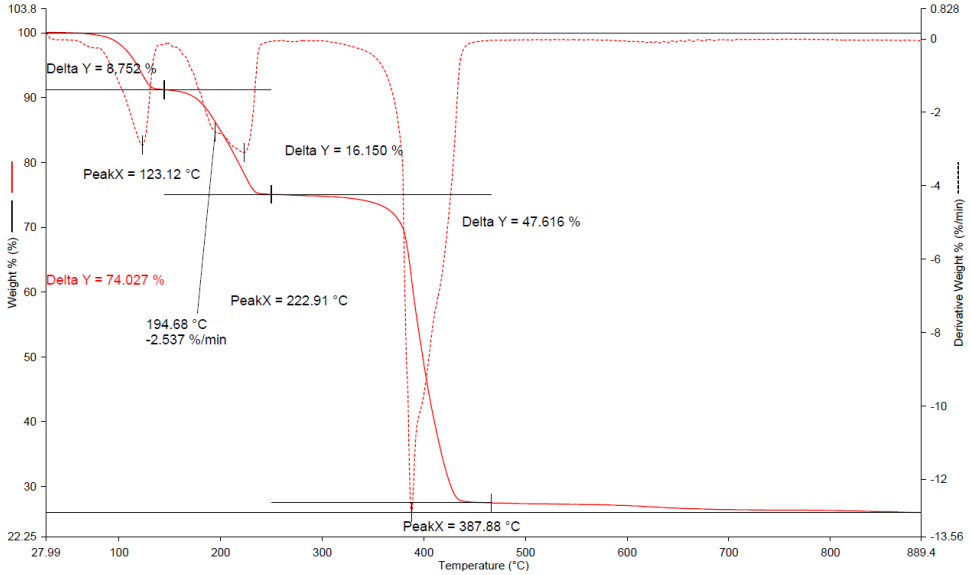

Fig. 5 The TG curve of Ru1.

Thermal analysis by the DSC method

The results of DSC show that during cooling, the allyl alcohol oligomer changes from the elastic state to the glassy within the range from −136 to −125.6 °C (ΔCp = 0.212 J g^{-1} K^{-1}) (Fig. S19). The transition from the glassy to the elastic state during heating occurs at T = −119.4 °C. At T = 95.7 °C on the DSC curves, one can observe a great exothermic process (1.763 mW mg^{-1}) related to thermal cross-linking of the allyl alcohol oligomer, the maximum value of which reaches T = 145.4 °C, a manifestation of a degradation, deoligomerization, or destruction reaction. The large change in enthalpy of this process indicates that the process is proceeding with considerable efficiency. The thermally cross-linked allyl alcohol oligomer decomposes thermally at T = 209.6 °C (0.8641 mW mg−1).39 The distribution of the examined sample of 2-chloro-2-propen-1-ol oligomer on the DSC curve (Fig. S20) is written in the form of a large exothermic signal, with a maximum at T = 129.2 °C (1.671

mW mg^{-1}). Another, the lesser exothermic signal at about 180 °C (1.022 mW mg−1), can probably be attributed to the flammability of the residue after the thermal decomposition of the oligomer. By analyzing the cooling curve, it can be concluded that the oligomer of 2-chloro-2-propen-1-ol changes from the elastic state to the glass state within the range from −131.6 to −123.2 °C (ΔCp = 0.127 J g^{-1} K^{-1}). The transition from glass to the elastic state during heating occurs at T = −121.6 °C. The glass-transition temperature for the 3-buten-2-ol oligomer is from −123.8 to −122.2 °C (ΔCp = 0.145 J g^{-1} K^{-1}) (Fig. S18). The transition from the glassy to the elastic state during heating occurs at T = −118.4 °C. At T = 87.7 °C, a great exothermic process can be observed, the maximum value of which reaches T = 142.3 °C (1.569 mW mg^{-1}). We observe a smaller exothermic peak at 360 °C (0.3323 mW mg^{-1}) and suppose that it is related to the flammability of the residue after the thermal decomposition of the oligomer.[40]

Next analysis of the DSC curve is devoted to the oligomer 2,3-dibromo-2-propen-1-ol, which changes from the elastic state to the glassy state from −111.9 to −102.4 °C (ΔCp = 0.231 J g^{-1} K^{-1}) (Fig. S19). The transition from glass to elastic during heating occurs at T = −97.6 °C. We can observe two exothermic peaks: a smaller one at 87 °C (0.533 mW mg^{-1}) and a larger one at 199 °C (1.047 mW mg^{-1}), which indicates thermal crosslinking of the 2,3-dibromo allyl alcohol oligomer.

At 429.7 °C, the thermally cross-linked oligomer undergoes complete thermal decomposition.[41] For comparison, the oligomers presented in the literature are a kind of derivative of polyvinyl chloride (PVC),[42] the glass transition temperature of which ranges from 77 to 80 °C depending on the molecular weight. The exceptional difference is likely due to the oligomers described in the literature having much shorter oligomer chains than the polyvinyl chloride polymer.[43] The melting point of the ethylene oligomer occurs in two stages at T = 22.9 °C (at −12.56 mW) and T = 125.7 °C (at −12.43 mW). Analyzing the literature, it can be deduced that polyethylene degrades at T = 125–135 °C. The faster degradation may be related to the presence of numerous branches in the chain of the oligomeric material or the formation of lower molecular weight oligomers, which decompose at lower temperatures (Fig. S20).

FT-IR spectra of oligomers

FTIR analysis of the oligomers confirms their structures (Fig. S24–S28). The FTIR spectra lead to the conclusion that the bands around 3300 cm^{-1} are a confirmation of strong –OH stretching vibrations, and the bands around 3000 cm^{-1} are attributed to asymmetric –CH stretching vibrations in the oligomer chain. Very weak bending vibrations of $–CH_2$ in the oligomer chain are confirmed by the band at approximately 1500 cm^{-1}. Vibrations at approximately 1000–1100 cm^{-1} were visualized, which confirmed the presence of C–O stretching vibrations.[44] In turn, the band at 750 cm^{-1} confirms the presence of –CH rocking vibrations.

The morphology of oligomers

The morphology of the obtained oligomers visualized using the SEM technique is presented in Fig. 6a–i. The allyl alcohol oligomer consists of aggregated sponge-like particles of a few micrometers in size. The morphologies of ethylene (Fig. S30), 2-chloro-2-propen-1-ol, 3-buten-2-ol, and 2,3-dibromo-2- propen-1-ol are different from those of the allyl alcohol oligomer, where it has the surface of irregular, corrugated and slightly wrinkled sheets. The SEM analysis was also applied to observe the ruthenium(III) complex. The morphology of the received complex is irregular with a smooth surface. There are grains of average size from a few to several dozen micrometers. The conclusions from the present study are consistent with the literature data, as the ethylene and 2-chloro-2-propen-1-ol oligomers studied by Malinowski et al. also had a heterogeneous and highly coagulated surface.[45]

The BET and Langmuir surface area of the obtained oligomeric materials

The BET isotherms are shown in Fig. 7, while Table 4 presents the details. The ethylene and allyl alcohol oligomers showed the highest specific surface area (168.8 and 124.7 m^2 g^{-1}, respectively). This is probably because both oligomers consist of the highest number of mers. The subsequent polar oligomers show similar specific surface areas ranging from 22 m^2 g^{-1} for the 2-chloro-2-propen-1-ol oligomer to 12 m^2 g^{-1} for the 3-buten-2-ol oligomer.

The degree of nitrogen adsorption in the ethylene oligomer was maintained at 100 cm^3 g^{-1} at 0.92 p/po, eventually reaching a nitrogen saturation of about 550 cm^3 g^{-1} at p/p0. The nitrogen saturation values at p/po for the subsequent oligomers are 160 cm^3 g^{-1} (allyl alcohol), 38 cm3 g−1 (2-chloroallyl alcohol), 18 cm^3 g^{-1} (2,3-dibromoallyl alcohol) and 11 cm^3 g^{-1} (3-buten-2-ol), respectively. The pore volume of the obtained oligomeric materials decreased with the specific gravity (range 0.84–0.016 cm^3 g^{-1}).[46]

Table 4 The BET and Langmuir surface area, pore volume and pore diameter of the obtained oligomeric materials

				HK/SF Micropore analysis	
Oligomer	BET surface area (m^2 g^{-1})	Langmuir surface area (m^2 g^{-1})	Total pore volume (cm^2 g^{-1})	Most frequent pore diameter (nm)	Median pore diameter (nm)
Ethylene	168.76	283.6	0.84	0.975	0.75
Allyl alcohol	124.65	396.1	0.26	0.61	0.66
2-Chloro-2-propen-1-ol	22.33	34.8	0.062	0.24	1.12
2,3-Dibromo-2-propen-1-ol	16.64	17.7	0.03	0.78	1.13
3-Buten-2-ol	12.22	5.2	0.016	1	1.14

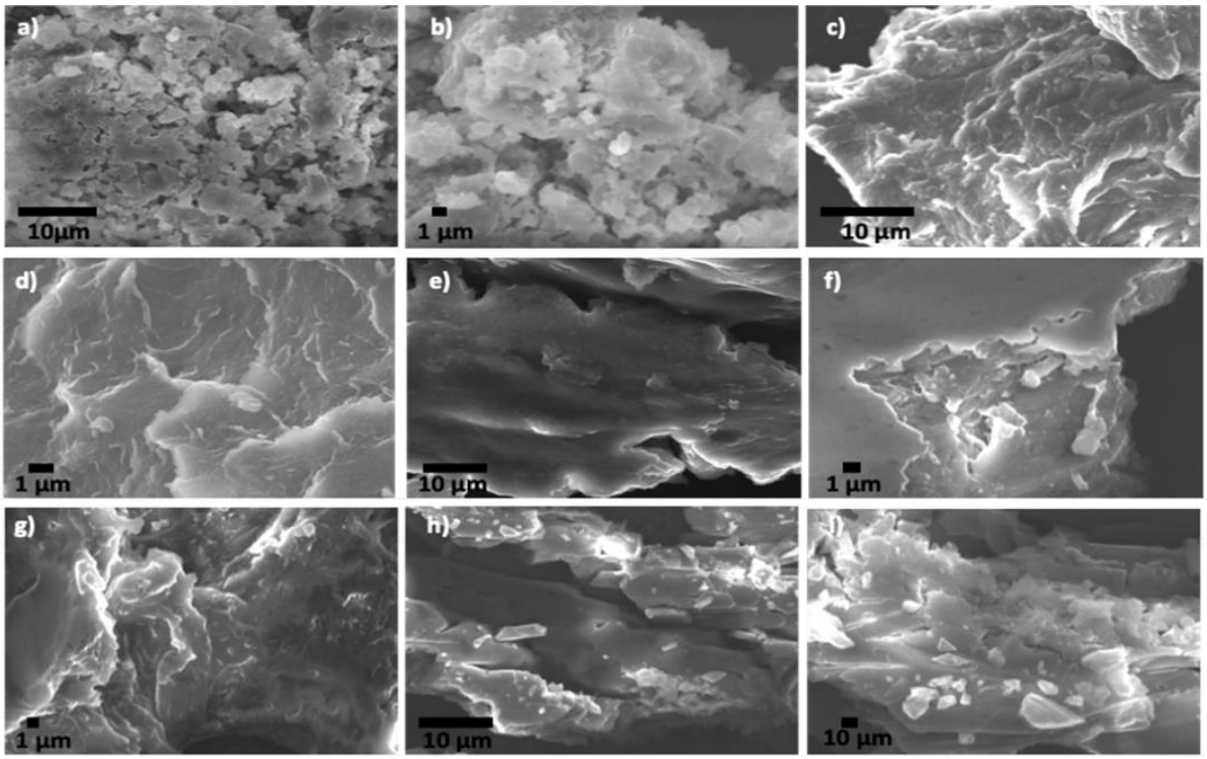

Fig. 6. SEM images of allyl alcohol oligomer (a-b), 2-chloro-2-propen-1-ol oligomer (c-d), 3-buten-2-ol oligomer (e-f), 2,3-dibromo-2-propen-1-ol oligomers (g), ruthenium(III) complex (h-i).

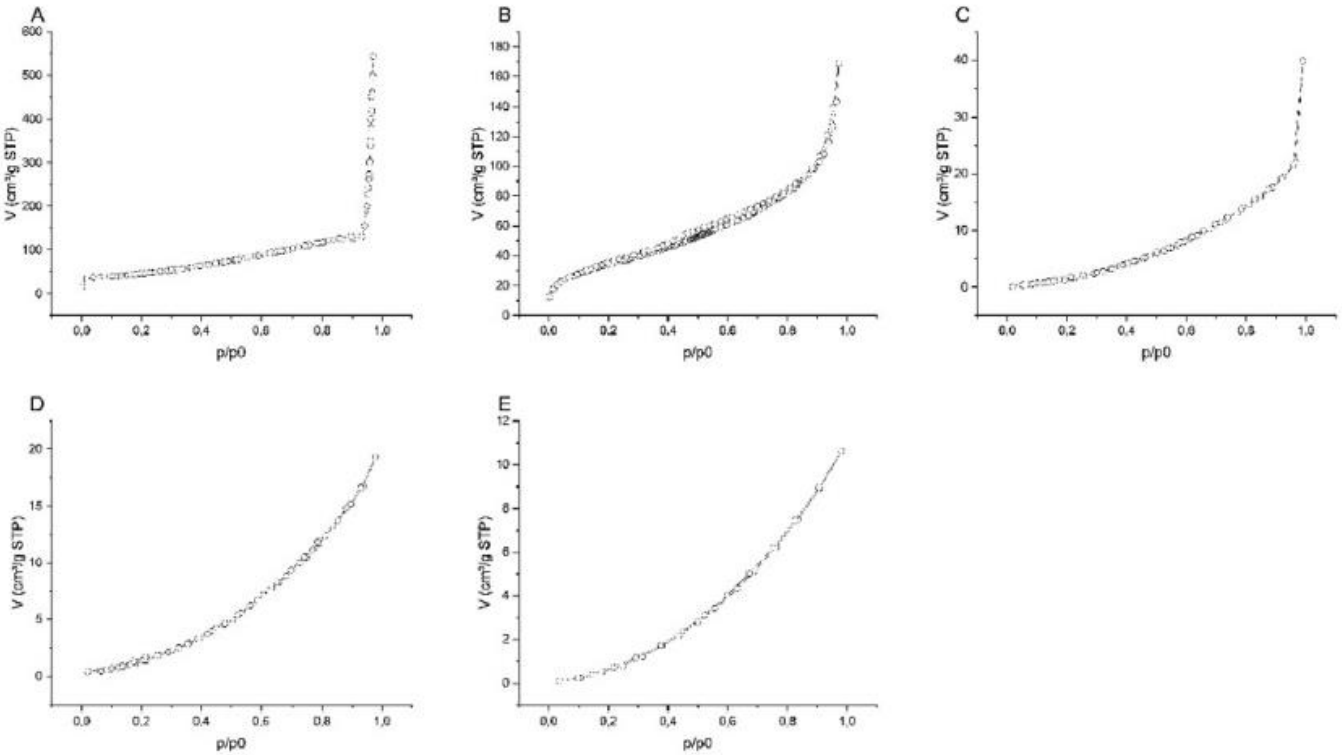

Fig. 7. BET isotherms of ethylene (A), allyl alcohol (B), 2-chloro-2-propen-1-ol (C), 2,3-dibromo-2-propen-1-ol (D), and 3-buten-2-ol oligomers (E).

Catalytic activity of Ru1

In the final part of the research, the catalytic activities (Ca) of the synthesized complex compound as a precatalyst were determined using the formula (Tables S2 and S5):[4,5]

$$Ca = \frac{m_o}{n_{Ru} t_p}$$

where mo = the weight of the oligomer sample (g), nRu = the number of mmol of ruthenium(III) ions used in the oligomerization process (mmol), t = the time of carrying out the oligomerization process (h) and p = the pressure of ethylene (bar). Table S2 shows the optimization of the oligomerization process of allyl alcohol and ethylene. The variable parameters were Al : Ru(III) molar ratio, temperature, and pressure. Since the other polar monomers show structural similarity to allyl alcohol, the oligomerization process of 2-chloro-2-propen-1-ol, 3-buten-2-ol, and 2,3-dibromo-2-propen-1-ol was carried out under the same conditions under which the highest catalytic activity was obtained in the oligomerization reaction of 2-propen-1-ol, i.e. T = 70 °C, Al : Ru(III) molar ratio 1 : 1500, amount of precatalyst: 3 µmol. In contrast, the highest catalytic activity in the ethylene oligomerization reaction was achieved using the following process conditions: p = 0.5 bar, T = 30 °C, Al:Ru(III) molar ratio 1 : 1500, precatalyst amount: 3 µmol.

The catalytic activity of the newly discovered, organometallic compound is in the range from 159.5 to 755.6 gmmol^{-1} h^{-1} bar^{-1}. Thus, it can be concluded that Ru1 is a highly active catalytic material (Table 5).

In addition, the values of TON – a maximum value of monomer conversion per unit of catalyst, where this parameter allows estimation of the catalyst lifetime and TOF (TON h^{-1}) – were determined. The highest conversion of monomer to oligomer was obtained in the ethylene oligomerization reaction, while the lowest was in the 2-chloro-2-propen-1-ol oligomerization reaction.

Since there are very few ruthenium(II/III/IV) precatalysts used in the polymerization of olefins, and if there are, most authors do not report the catalytic activity, and the comparative analysis is not very extensive, Fig. S31 compares the catalytic properties of ruthenium(II) and ruthenium(III) complex compounds in ethylene oligomerization and polymerization. Because the authors provide catalytic activity in different units, the values given in the literature have been converted to g mmol^{-1} h^{-1} bar^{-1}. The newly synthesized Ru(III) compound in coordination with 2-phenylpyridine is the most active Ru(II/III/IV) precatalyst in the ethylene oligomerization reaction that has been synthesized so far. Compared to the studies of the Camacho-Fernandez group, the catalytic activity of Ru1 is almost 21 times higher than the metallocene complex of Ru(II) with the N-donor ligand and more than 53-fold higher than the S-donor analog his group synthesized.

Despite the low steric hindrance around the active centre due to the presence of DMSO and NO, the enhanced catalytic activity can be attributed to the electron properties of the ruthenium(III) coordination compound due to the presence of the C,N-donor ligand (2-phenylpyridine). The enhanced catalytic properties compared to known Ru(II/III) precatalysts can probably be attributed to increased intramolecular charge transfer, increased crystal field strength, and electron density around the ruthenium ion due to the presence of a carboanion in 2-phenylpyridine (Ru–C).47 Researchers' studies confirm the increased electron transfer (d → π*) and charge and energy separation properties on the donor orbital48 during the substitution of 2,2'- bipyridyl (N,N-donor) by 2-phenylpyridine (C,N-donor).[49] The observations indicate that the enhanced catalytic activity correlates with the strong donor character of 2-phenylpyridine and the increased electron density around the ruthenium ion.

For comparison, we would like to cite a few examples from the literature of the use of ruthenium coordination compounds as precatalysts in olefin polymerization, e.g. [Ru(PPh_3)$_3$(Cl)(H)], (PPh_3 = triphenylphosphine), which show very low activity in ethylene polymerization. In turn, Yamamoto et al.50 report that the polymerization of functionalized vinyl monomers by the [Ru(PPh_3)$_4$(H)$_2$], despite a similar structure to the previous compound, does not show the catalytic activity of ethylene polymerization. However, acrylonitrile is polymerized with 57% conversion within five minutes by this coordination compound. Ruthenium(II) catalysts of the ligand system [2,6-bis-[(4S)-4-isopropyl-2-oxazolin-2-yl]pyridine][19,20] in combination with MAO cocatalyst show moderate catalytic activity (10–100 g mmol^{-1} h^{-1})[4,5] for ethylene homopolymerization and ethylene/1-hexene copolymerization. In particular, ruthenium catalysts with a direct attachment of two atoms of chlorine, iodine or triflate anion (CF_3SO_3) show moderate catalytic activity for ethylene/1-hexene copolymerization with high yield.

Table 5 Summary of the catalytic activity of **Ru1** in selected monomers' oligomerization reaction (after optimisation studies)

Monomers	Activator	**Ru1** (mmol)	T (°C)	T_g[b] (°C)	T_m[b] (°C)	Yield (g)	TON[c]	TOF[d] (h^{-1})	C_a[e]	C_a[f] x10^5
Ethylene[a]	MAO	0.003	30	—	125.7	0.85	10 101.1	13 468	755.6	3.78
Allyl alcohol			70	−131.5	145.4; 209.6	0.64	3673.1	5509.6	318.4	3.18
2-Chloro-2-propen-1-ol				−126.4	129.2; 180	0.32	1154.7	1723.4	159.5	1.60
3-Buten-2-ol				−119.6	142.3; 360	0.40	1856.7	2228.9	161.2	1.61
2,3-Dibromo-2-propen-1-ol				−107.6	87; 199	1.21	1868.3	1868.3	403.3	4.03

The process was carried out at ambient pressure under mild conditions. The molar ratio of Ru^{3+}: Al (activator) in all cases is equal to 1 : 1500. [a] Ethylene pressure was equal to 0.5 bar. [b] Determined by the DSC analysis. [c] Mol. of the converted monomer mol^{-1} precatalyst. [d] TON h^{-1}. [e] g mmol^{-1} h^{-1} bar^{-1}. [f] g mol^{-1} h^{-1}.

Conclusions

In conclusion, a new well-defined ruthenium(III)-based complex compound has been designed, physicochemically characterized, and used in the oligomerization reactions of ethylene, allyl alcohol, 2-chloro-2-propen-1-ol, 3-butene-2-ol and 2,3-dibromo-2-propen-1-ol. The MAO-activated Ru(III)-based catalytic material showed high catalytic activity in the oligomerization reactions of the aforementioned olefins, as the catalytic activity values are in the range of 159.5–755.6 g $mmol^{-1}$ h^{-1} bar^{-1}. The structure, morphology, physicochemical, and thermal properties of the oligomeric materials were studied by several techniques, i.e., BET, MALDI-TOF-MS, FTIR, NMR, SEM, DSC, and TGA. The ethylene and allyl alcohol oligomer showed the highest specific surface area (168.8 and 124.7 m^2 g^{-1}, respectively). This is probably because both oligomers consist of the highest number of mers. On the other hand, the smallest specific surface area is characterized by the 3-buten-2-ol oligomer (12 m^2 g^{-1}).

Overall, the described organometallic compound is an innovative catalytic material for use in olefin oligomerisation due to its unprecedentedly high catalytic activity (755.6 g $mmol^{-1}$ h^{-1} bar^{-1}, TON = 10 101.1 and TOF = 13 468 h^{-1} in ethylene oligomerisation) under mild reaction conditions (i.e. 30 °C), which is rare. Additional advantages over metallocene catalysts include a simple, one-step synthesis and high physicochemical and thermal stability (up to 388 °C). So far, ruthenium(II/III/IV) ion-based precatalysts have exhibited low to moderate catalytic activity, so the research presented here represents a breakthrough step towards the further design of a new generation of highly stable ruthenium(III) ion-based catalytic materials with potential application in large-scale polymer production.

Author contributions

The manuscript was written through contributions of all authors. All authors have given approval to the final version of the manuscript. Conceptualization: K. P., J. D., and D. J.; methodology: K. P., J. D. and D. J. investigation: K. P., K. J., R. K., K. D., D. S., P. R., B. G., and A. G.; writing – original draft: K. P. K. J., and R. K.; writing – review and editing: K. P., K. J., R. K, and D. J.; project administration: K. P. and D. J.; funding acquisition: K. P.

Conflicts of interest

The authors declare no competing financial interest.

Acknowledgements

Publication financed from the state budget under the programme of the Ministry of Education and Science entitled Pearls of Science project no. PN/01/0137/2022, grant amount 0 PLN, total project value 239 800.00 PLN (Polska).

References

1 F. W. Michelotti and W. P. Keaveney, J. Polym. Sci., Part A, 1965, 3, 895–905.
2 M. Li, R. Wang, M. S. Eisen and S. Park, Org. Chem. Front., 2020, 7, 2088–2106.
3 M. A. Camacho-Fernandez, M. Yen, J. W. Ziller and Z. Guan, Chem. Sci., 2013, 4, 2902.
4 V. C. Gibson and S. K. Spitzmesser, Chem. Rev., 2003, 103, 283–316.
5 G. J. P. Britovsek, V. C. Gibson and D. F. Wass, Angew. Chem., Int. Ed., 1999, 38, 428–447.
6 K. Nomura and W. Zhang, Chem. Sci., 2010, 1, 161.
7 A. Ashuiev, F. Allouche, N. Wili, K. Searles, D. Klose, C. Copéret and G. Jeschke, Chem. Sci., 2021, 12, 780–792.
8 B. Gawdzik, J. Drzeżdżon, T. Siarhei, A. Sikorski, A. Malankowska, P. Kowalczyk and D. Jacewicz, Materials, 2021, 14, 7670.
9 E. Salvadori, M. Chiesa, A. Buonerba and A. Grassi, Chem. Sci., 2020, 11, 12436–12445.
10 D. Takeuchi, Dalton Trans., 2010, 39, 311–328.
11 H. M. Moura, N. L. Gibbons, S. A. Miller and H. O. Pastore, Dalton Trans., 2018, 47, 3128–3143.
12 B. Song, B. He, A. Qin and B. Z. Tang, Macromolecules, 2018, 51, 42–48.
13 S. E. Chérif, A. Ghosh, S. Chelli, I. M. Dixon, J. Kraiem and S. Lakhdar, Chem. Sci., 2022, 13, 12065–12070.
14 C. Wang, S. Friedrich, T. R. Younkin, R. T. Li, R. H. Grubbs, D. A. Bansleben and M. W. Day, Organometallics, 1998, 17, 3149–3151.
15 K. Noura, S. Warit and Y. Imanishi, Macromolecules, 1999, 32, 4732–4734.
16 E. L. Dias, M. Brookhart and P. S. White, Organometallics, 2000, 19, 4995–5004.
17 F. Simal, A. Demonceau and A. F. Noels, Angew. Chem., Int. Ed., 1999, 38, 538–540.
18 T. Yamamoto, S. Miyashita, Y. Naito, S. Komiya, T. Ito and A. Yamamoto, Akio Yamamoto, 1982, 808–812.
19 S. Koiya and A. Yamamoto, Bull. Chem. Soc. Jpn., 1976, 49, 2553–2559.
20 K. Nomura, W. Sidokmai and Y. Imanishi, Bull. Chem. Soc. Jpn., 2000, 73, 599–605.
21 M. A. Spackman, Phys. Scr., 2013, 87, 048103.
22 M. A. Spackman and P. G. Byrom, Chem. Phys. Lett., 1997, 267, 215–220.
23 M. A. Spackman and D. Jayatilaka, CrystEngComm, 2009, 11, 19–32.
24 Y. Ohashi, Acta Crystallogr., Sect. A: Found. Crystallogr., 1998, 54, 842–849.

25 D. Schaniel, N. Casaretto, E.-E. Bendeif, T. Woike, A. K. E. Gallien, P. Klüfers, S. E. Kutniewska, R. Kamiński, G. Bouchez, K. Boukheddaden and S. Pillet, CrystEngComm, 2019, 21, 5804–5810.
26 A. A. Mikhailov, G. A. Kostin and D. Schaniel, New J. Chem., 2022, 46, 12641–12650.
27 C. F. Macrae, I. J. Bruno, J. A. Chisholm, P. R. Edgington, P. McCabe, E. Pidcock, L. Rodriguez-Monge, R. Taylor, J. van de Streek and P. A. Wood, J. Appl. Crystallogr., 2008, 41, 466–470.
28 A. Kobayashi, K. Komatsu, H. Ohara, W. Kamada, Y. Chishina, K. Tsuge, H.-C. Chang and M. Kato, Inorg. Chem., 2013, 52, 13188–13198.
29 J. Rack, Coord. Chem. Rev., 2009, 253, 78–85.
30 M. Y. Livshits, L. Wang, S. B. Vittardi, S. Ruetzel, A. King, T. Brixner and J. J. Rack, Chem. Sci., 2020, 11, 5797–5807.
31 C. Copéret, A. Comas-Vives, M. P. Conley, D. P. Estes, A. Fedorov, V. Mougel, H. Nagae, F. Núñez-Zarur and P. A. Zhizhko, Chem. Rev., 2016, 116, 323–421.
32 D. A. Lutterman, A. A. Rachford, J. J. Rack and C. Turro, J. Phys. Chem. A, 2009, 113, 11002–11006.
33 D. Schaniel and T. Woike, Phys. Chem. Chem. Phys., 2009, 11, 4391.
34 N. Casaretto, S. Pillet, E.-E. Bendeif, D. Schaniel, A. K. E. Gallien, P. Klüfers and T. Woike, Acta Crystallogr., Sect. B: Struct. Sci., Cryst. Eng. Mater., 2015, 71, 788–797.
35 I. S. Fomenko, A. A. Mikhailov, V. Vorobyev, N. V. Kuratieva, G. A. Kostin, D. Schaniel, V. A. Nadolinny and A. L. Gushchin, J. Photochem. Photobiol., A, 2021, 407, 113044.
36 R. L. Hudson, M. J. Loeffler and P. A. Gerakines, J. Chem. Phys., 2017, 146, DOI: 10.1063/1.4973548.
37 G. Janowska, A. Kucharska-Jastrząbek and P. Rybiński, J. Therm. Anal. Calorim., 2011, 103, 1039–1046.
38 P. Rybiński, G. Janowska, M. Jóźwiak and A. Pająk, J. Therm. Anal. Calorim., 2012, 107, 1243–1249.
39 G. Janowska, P. Rybiński and R. Jantas, J. Therm. Anal. Calorim., 2007, 87, 511–517.
40 G. Janowska and P. Rybiński, J. Therm. Anal. Calorim., 2008, 91, 697–701.
41 J. Miedzianowska, M. Masłowski, P. Rybiński and K. Strzelec, Materials, 2020, 13, 4163.
42 J. Drzeżdżon, B. Gawdzik, P. Rybiński, J. Malinowski and D. Jacewicz, J. Therm. Anal. Calorim., 2021, 146, 1623–1627.
43 M. Urbaniak, K. Pobłocki, P. Kowalczyk, K. Kramkowski, J. Drzeżdżon, B. Gawdzik, P. Świtała, M. Miler, D. Heleniak, P. Rybiński and D. Jacewicz, Molecules, 2022, 27, 8038.
44 K. Pobłocki, J. Drzeżdżon, B. Gawdzik and D. Jacewicz, Green Chem., 2022, 24, 9402–9427.
45 J. Malinowski, D. Jacewicz, A. Sikorski, M. Urbaniak, P. Rybiński, P. Parnicka, A. Zaleska-Medynska, B. Gawdzik and J. Drzeżdżon, Sci. Rep., 2021, 11, 15212.
46 M. A. Baluk, P. Mazierski, A. Pieczyńska, K. Nikiforow, G. Trykowski, T. Klimczuk and A. Zaleska-Medynska, Catal. Sci. Technol., 2023, 13, 5033–5047.
47 L. Labat, J. Lamère, I. Sasaki, P. G. Lacroix, L. Vendier, I. Asselberghs, J. Pérez-Moreno and K. Clays, Eur. J. Inorg. Chem., 2006, 2006, 3105–3113.
48 E. C. Constable and C. E. Housecroft, Polyhedron, 1990, 9, 1939–1947.
49 J.-P. Collin, M. Beley, J.-P. Sauvage and F. Barigelletti, Inorg. Chim. Acta, 1991, 186, 91–93.
50 S. Komiya and A. Yamamoto, J. Mol. Catal., 1979, 5, 279– 292.

Supporting Information

Porous oligomeric materials synthesised using a new, highly active precatalyst based on ruthenium(III) and 2-phenylpyridine

Kacper Pobłocki, *[a] Katarzyna N. Jarzembska,[b] Radosław Kamiński,[b] Joanna Drzeżdżon,[a] Krystyna A. Deresz,[b] Dominik Schaniel,[c] Anna Gołąbiewska,[a] Barbara Gawdzik,[d] Przemysław Rybiński[d] and Dagmara Jacewicz *[a]

Experimental

Materials

Almost all chemical compounds (except $RuCl_3NO$) were purchased from Merck, Darmstadt, Germany: 2-phenylpyridine (98% purity), toluene (99.5% purity), dimethyl sulfoxide (DMSO) (99.8% purity), hexane (99% purity), methylaluminoxane (MAO), ethylaluminium dichloride ($AlEtCl_2$), 2-propen-1-ol (98.5% purity), 2-chloro-2-propen-1-ol (90% purity), 3-buten-2-ol (97% purity), 2,3-dibromo-2-propen-1-ol (90% purity). $RuCl_3NO$ was purchased from BDH British Drug Houses, England (Fig. S29).

Complex compound synthesis

The **Ru1** compound is designed according to the principle of hard and soft Lewis acids and bases. **Ru1** was synthesized by adding 0.840 mL of 2-phenylpyridine (6 mmol) to 0.207 grams (1 mmol) of $RuCl_3NO$. Then 30 mL of H_2O/DMSO solution (v:v) was added to the flask and the mixture was heated for 2 hours under reflux until the solution turned scarlet. After one hour of heating, 20 mL of H_2O/DMSO (v:v) was added. After 14 days a single crystalline product was obtained.

Elemental analysis: C13H14O2N2RuCl2S; calculated: C 35.95%, H 3.25%, N 6.45%; found: C 36.11%, H 3.09%, N 6.29%.

Elemental analysis

Elemental analysis was carried out with an Elementar Vario EL III analyzer.

X-ray diffraction

Single-crystal X-ray measurement was performed on a Rigaku Oxford Diffraction SuperNova instrument equipped with a microfocus molybdenum X-ray source (Mo K_α radiation, λ = 0.71073 Å). During the measurement, a crystal was maintained at 100 K with the use of an Oxford Cryosystems nitrogen gas-flow device. Unit-cell parameter determination and raw diffraction image processing were performed with the native diffractometer *CRYSALISPRO* software suite. The structure was solved using an intrinsic phasing method as implemented in the *SHELXT* program[1] and refined with the *JANA* package[2] within the independent atom model approximation. The hydrogen atoms were placed geometrically with the riding model for the hydrogen thermal motion parameters applied (d_{C-H} = 0.96 Å, $U_{iso}^H = 1.2 \cdot U_{eq}^C$). The respective CIF files are available from the Supporting Information or can be retrieved from the Cambridge Structural Database[3,4] (deposition number: CCDC 2193867).

Spectroscopy

Almost all infrared (IR) measurements were performed using a Nicolet 5700 FTIR spectrometer (spectral resolution of 2 cm^{-1} in the range of 360–4000 cm^{-1}) equipped with a closed-cycle cryostat (Oxford Optistat V01). The sample was grinded, mixed with a spectroscopic-grade KBr, pressed into pellets, and glued to the cold finger of the cryostat using silver-paste thermal adhesive. During measurements, the sample was kept in a vacuum inside the cryostat. Irradiation of the sample was achieved through the cryostat window using various LEDs (Thorlabs L and LP series). IR spectra of oligomers were recorded ranging from

4000 to 400 cm^{-1} in KBr pellet (BRUKER IFS 66 spectrophotometer). Each spectrum consisted of 64 scans.

Computational analysis

All computations were carried out using the *GAUSSIAN* package (ver. 16) [5]. Molecule optimizations, isolated-molecule geometry optimizations, normal-mode frequencies and dimer interaction energies were calculated at the DFT(B3LYP)/6-311++G** level of theory [6–11]. For harmonic mode computations, no imaginary frequencies were found. In the case of interaction energy calculations, the Grimme empirical dispersion correction [10,11], modified by the Becke-Johnson damping function 34,35, and correction for basis set superposition error [14,15] were applied. The semi-automatic generation of input files was accomplished with the *CLUSTERGEN* program [16–18].

Oligomerization process

The oligomerization process of monomers was carried out in a glass vial with a silicon stopper to close off the air supply to the reaction mixture. First, 3 μmol of **Ru1** precatalyst were dissolved in a 2 mL mixture of toluene. The solution was then stirred for 15 minutes until the complex compound was completely dissolved. In the next step, an appropriate amount (optimization) of methylaluminoxane (MAO), which acted as an activator, and 3 mL of monomer (2-propen-1-ol/2-chloro-2-propen-1-ol/3-buten-2-ol/2,3-dibromo-2-propen-1-ol) were added. On the other hand, during ethylene oligomerization, the monomer was introduced from a cylinder at a pressure of 0.3/0.5/0.8 bar. All oligomerization reactions were carried out at atmospheric pressure, at 30°C, 50°C, or 70°C, under a nitrogen atmosphere. After completion of the oligomerization process, the resulting gels were washed with a mixture of hydrochloric acid and methanol (in a molar ratio of 1:1) to get rid of the precatalyst residue. The oligomeric material was dried to a constant weight, then weighed and physicochemical analyses were performed. MALDI-TOF-MS, TGA, DSC, FTIR, and SEM analyses were performed for the oligomerization reaction products in which the highest catalytic activity was obtained.
Identical tests were performed with ethylaluminum dichloride as an activator, using *n*-hexane as solvent (instead of MAO as activator and toluene as solvent). However, the resulting gels were completely decomposed after washing with a mixture of acid and methanol, so they were not subjected to further physicochemical analyses.

MALDI-TOF-MS

The MALDI-TOF-MS spectra were recorded on the Bruker Biflex III company, (Branch Überlingen, Germany). 2,5-Dihydroxybenzoic acid (DHB) was used as a matrix.

Thermal analysis (TG)

TG was performed on NETZSCH TG 209 instrument in an argon atmosphere temperature range from 0 to 1000°C. The mass of samples subjected to thermal analysis was about 5 mg.

Differential scanning calorimetry (DSC)

DSC studies were performed using the equipment from Mettler Toledo in the range from − 150 to 500°C with a heating rate of 10 °C·min^{-1} in the inert atmosphere. The sample for the DSC measurements was about 5 mg.

Scanning Electron Microscope (SEM)

The morphology of the prepared Ru1 and oligomers was investigated using a field-emission scanning electron microscope (SEM). For sample preparation, a certain amount of the powder was deposited onto carbon tape and was imaged with JEOL JSM-7610 F operating at 15 kV.

The BET and Langmuir surface area

The BET and Langmuir surface area study was determined using sorption analyzer 3P Instrument Micro 200 in data collecting of BET surface area, isotherm, pore size, and volume. Total pore volume was calculated at pressure p/p0 = 0.99. Pore size distribution was calculated using the Horvath-Kawazoe / Saito-Foley (HK/SF) method was calculated using the 3P-Instrument PAS program.

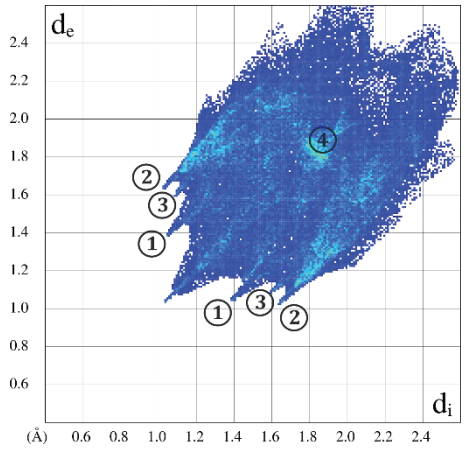

Figure S1. Hirshfeld fingerprint plot generated for the **Ru1** crystal structure; selected interatomic contact types are denoted with numbers: 1 – O···H, 2 – Cl···H, 3 – C···H, 4 – π···π.

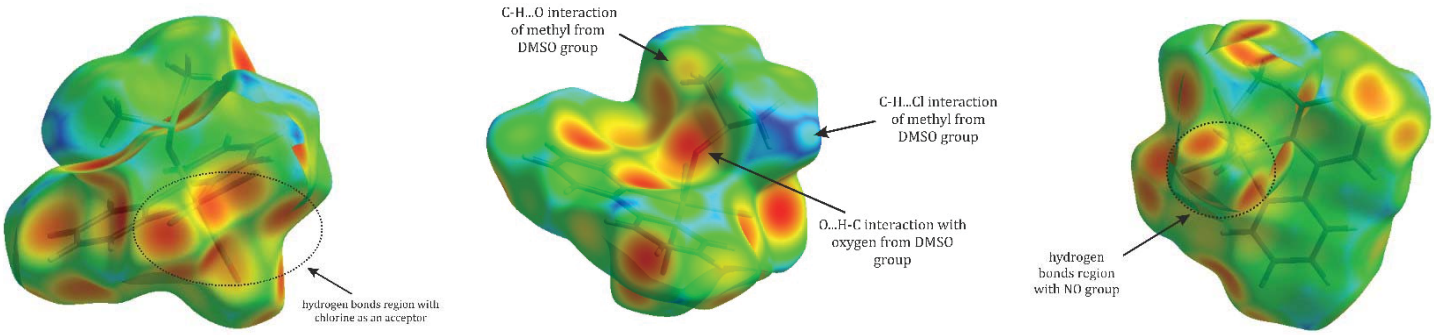

Figure S2. Hirshfeld surfaces with the d_e property mapped onto (1.03−2.69 Å range) illustrating hydrogen bonds in the analyzed crystal structure of **Ru1**.

Table S1. Reaction cavities determined for the NO and DMSO ligands based on selected structures retrieved from the Cambridge Structural Database (with *R*-factor < 5%), or from literature. In the case of the NO ligand, the cavities were calculated for structures known to be switchable under light irradiation.

REFCODE / Reference	*Ligand*	*Cavity volume,* V_{cav} / Å^3
Schaniel *et al.*[19]	NO	17.4
Mikhailov *et al.*[20]		23.6
CDMSOR10	O-bound DMSO	100.5
CDMSOR08		88.3
HALZUS		93.4
MEYZIC		109.2
CDMSOR10	S-bound DMSO	91.5
ATUNOU		115.3
CDMSOR08		95.6
HALZUS		96.1
MEYZIC		92.4

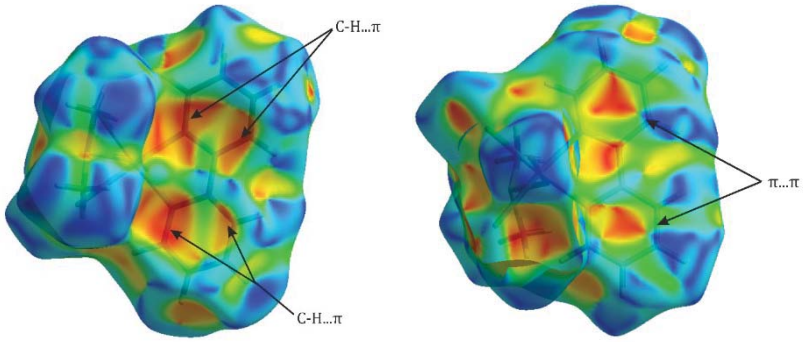

Figure S3. Shape index (from –1.0 to 1.0 a.u.) mapped onto the Hirshfeld surfaces which illustrates well C–H···π and π-stacking interactions in the analyzed crystal structure of **Ru1**.

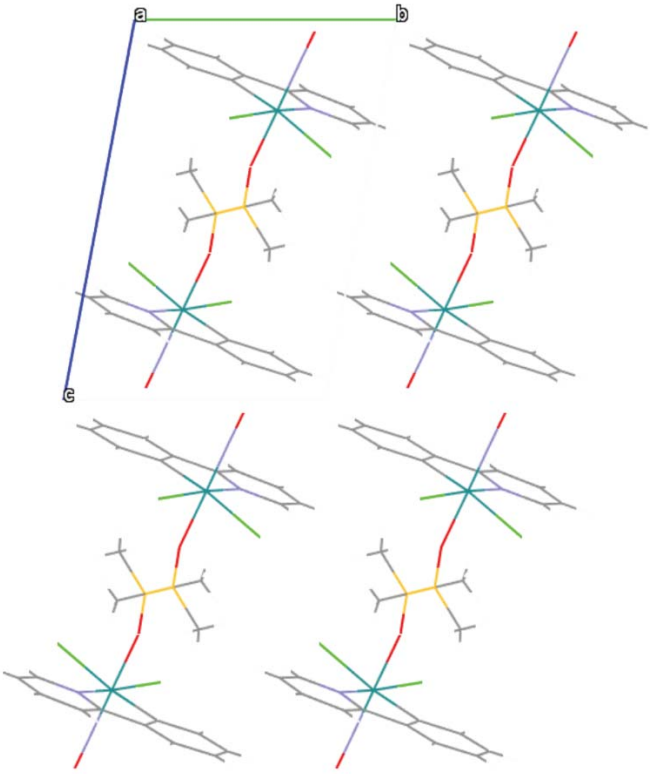

Figure S4. Crystal packing of **Ru1** (view along the *X*-axis).

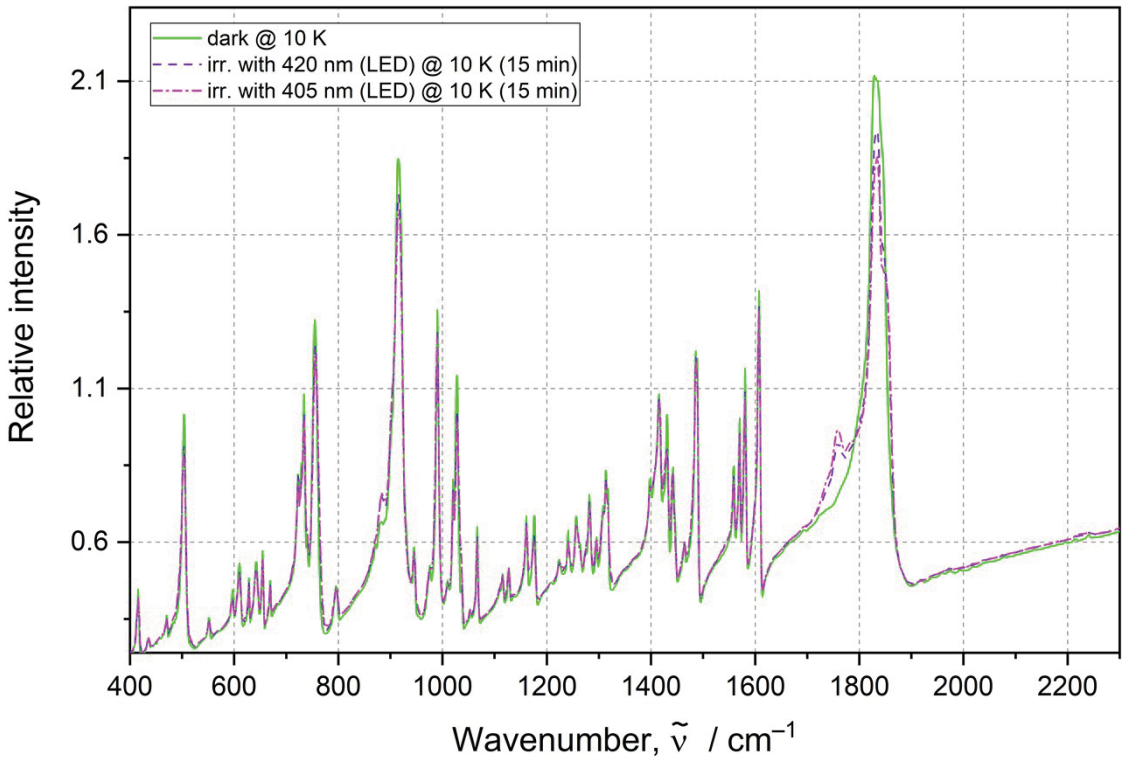

Figure S5. IR spectra collected at 10 K: no irradiation (green solid line), after irradiation with the 420 nm LED for 15 min. (violet dashed line), after irradiation with the 405 nm LED for 15 min. (magenta dashed-dotted line).

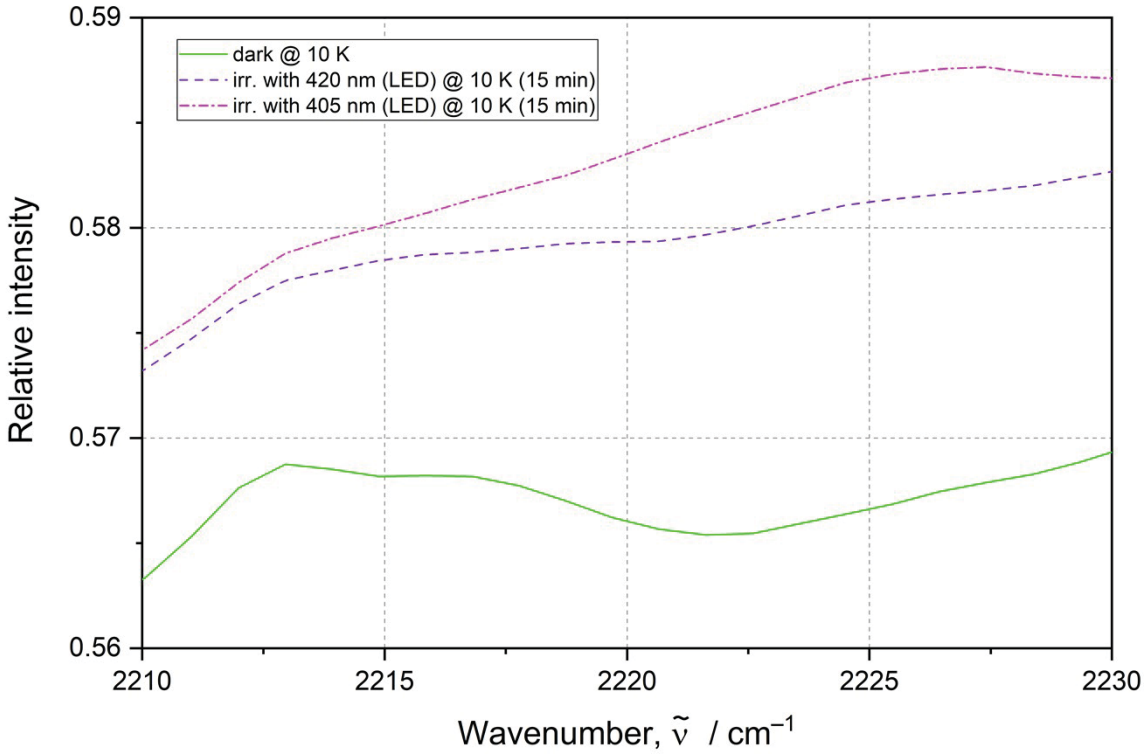

Figure S5 (continued). IR spectra collected at 10 K: no irradiation (green solid line), after irradiation with the 420 nm LED for 15 min. (violet dashed line), after irradiation with the 405 nm LED for 15 min. (magenta dashed-dotted line).

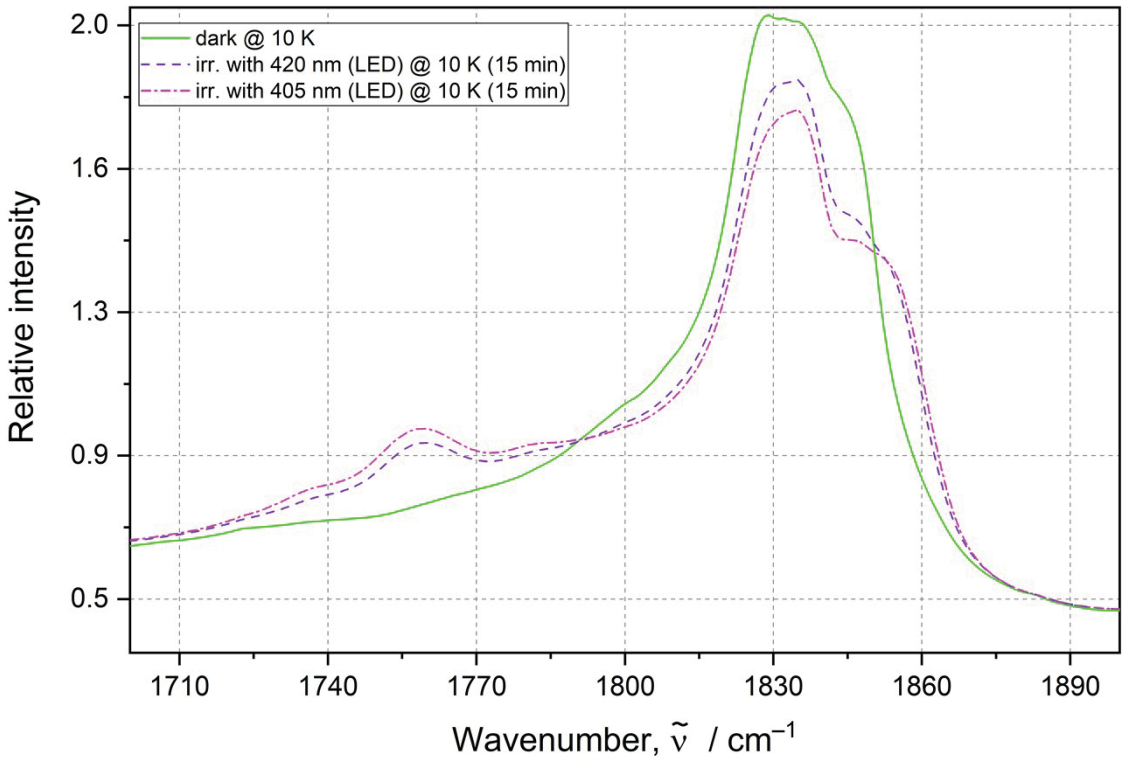

Figure S5 (continued). IR spectra collected at 10 K: no irradiation (green solid line), after irradiation with the 420 nm LED for 15 min. (violet dashed line), after irradiation with the 405 nm LED for 15 min. (magenta dashed-dotted line).

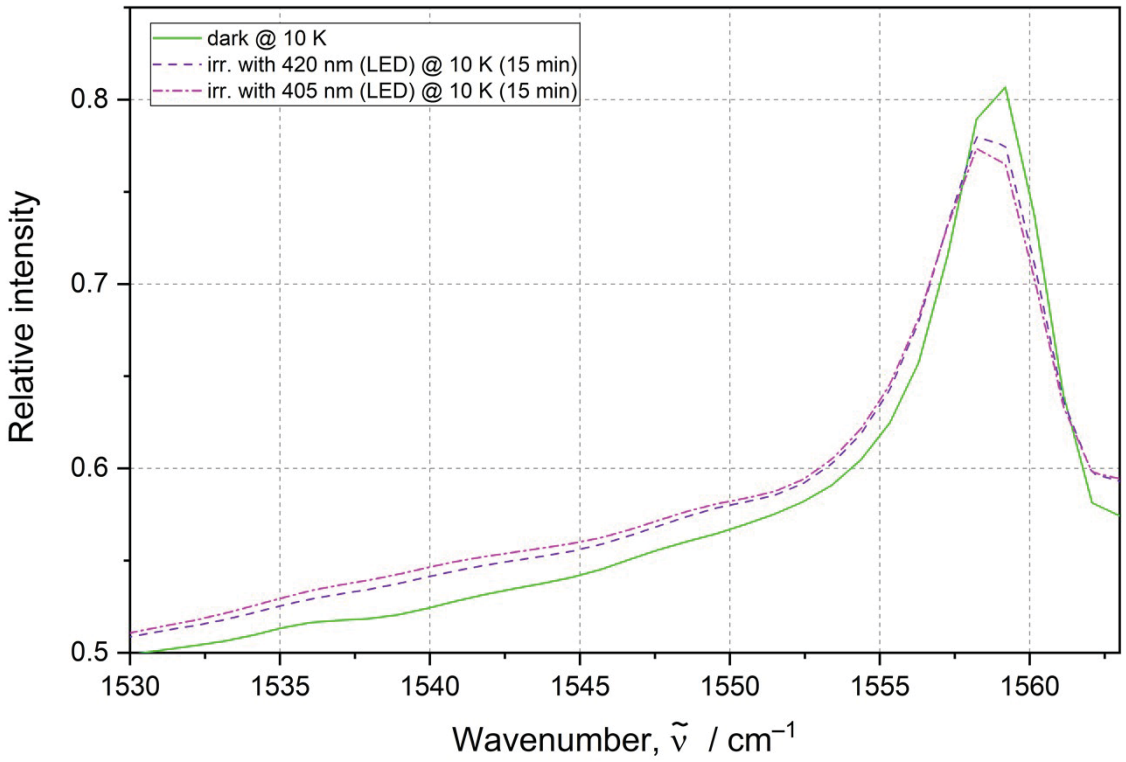

Figure S5 (continued). IR spectra collected at 10 K: no irradiation (green solid line), after irradiation with the 420 nm LED for 15 min. (violet dashed line), after irradiation with the 405 nm LED for 15 min. (magenta dashed-dotted line).

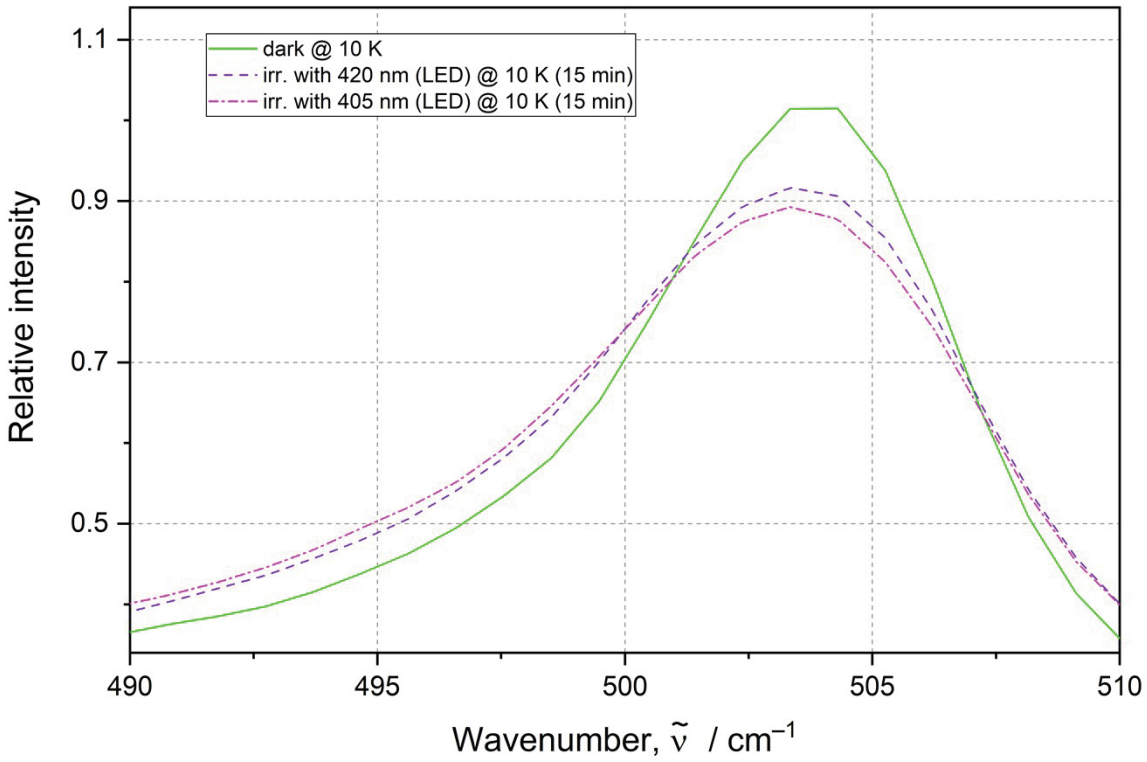

Figure S5 (continued). IR spectra collected at 10 K: no irradiation (green solid line), after irradiation with the 420 nm LED for 15 min. (violet dashed line), after irradiation with the 405 nm LED for 15 min. (magenta dashed-dotted line).

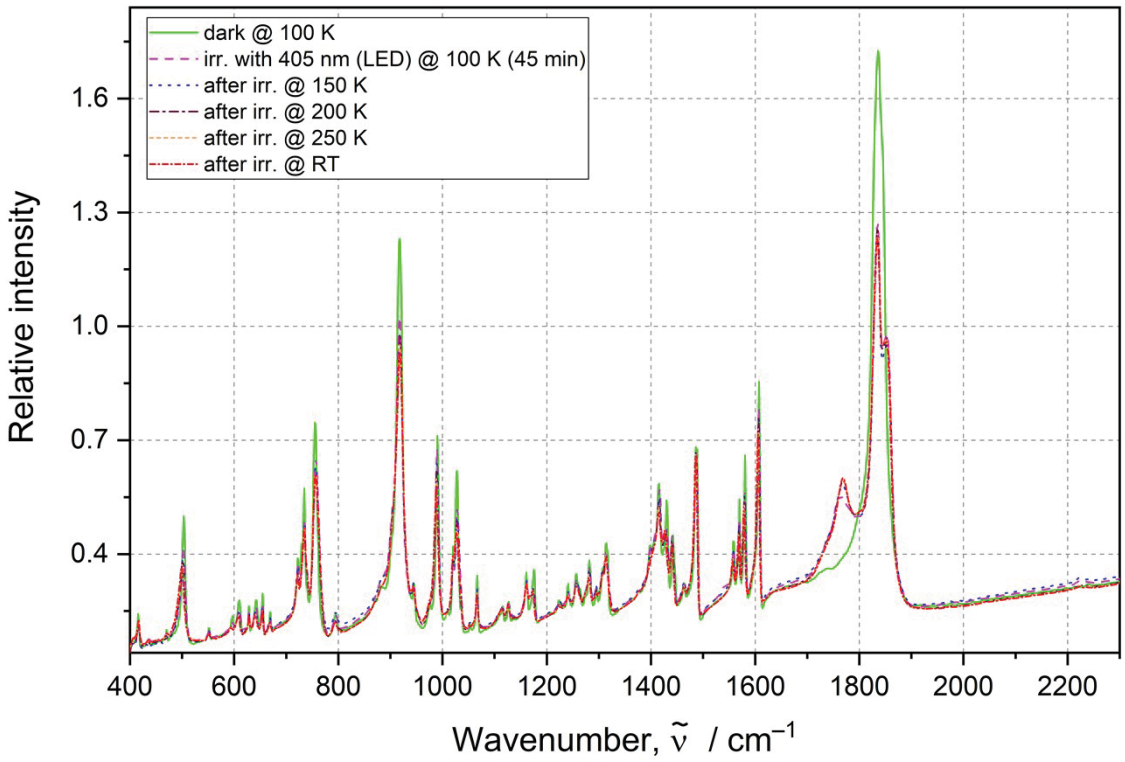

Figure S6. IR spectra collected at with no irradiation (green solid line) at 100 K, after irradiation with the 420 nm LED for 45 min. at 100 K (violet dashed line), and during temperature increasing: at 150 K (blue dotted line), at 200 K (brown dashed-dotted line), at 250 K (orange short dotted line) and at RT (red short dotted-dashed line).

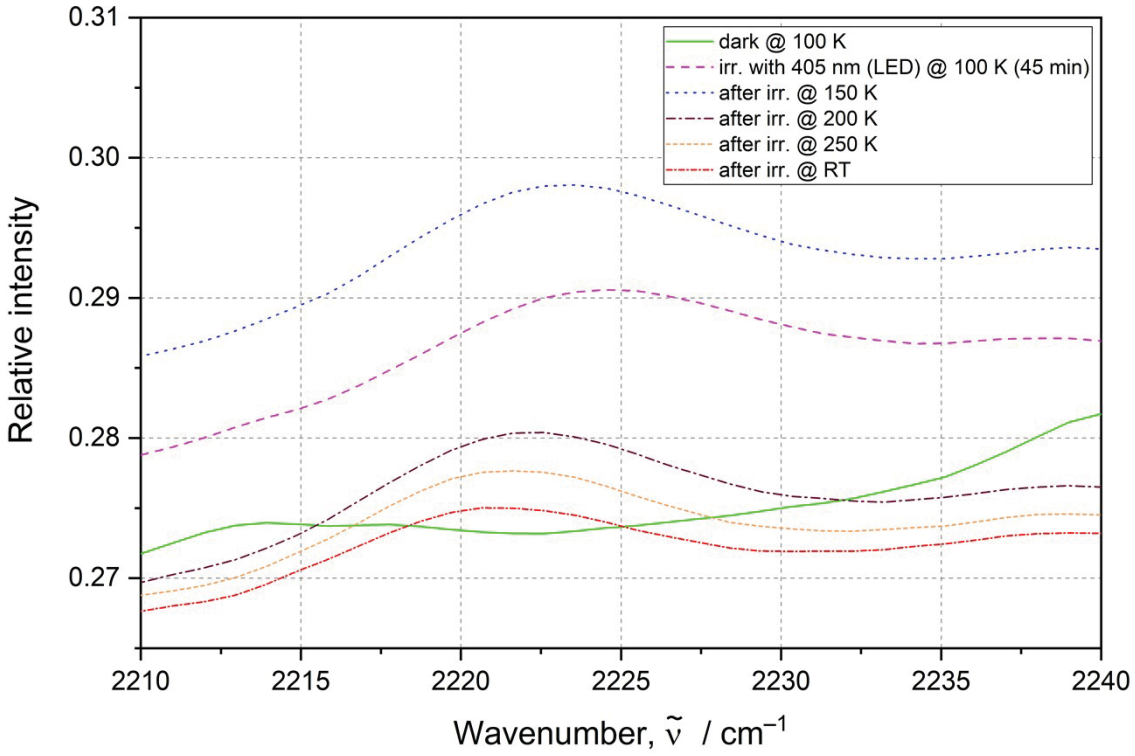

Figure S6 (continued). IR spectra collected at with no irradiation (green solid line) at 100 K, after irradiation with the 420 nm LED for 45 min. at 100 K (violet dashed line), and during temperature increasing: at 150 K (blue dotted line), at 200 K (brown dashed-dotted line), at 250 K (orange short dotted line) and at RT (red short dotted-dashed line).

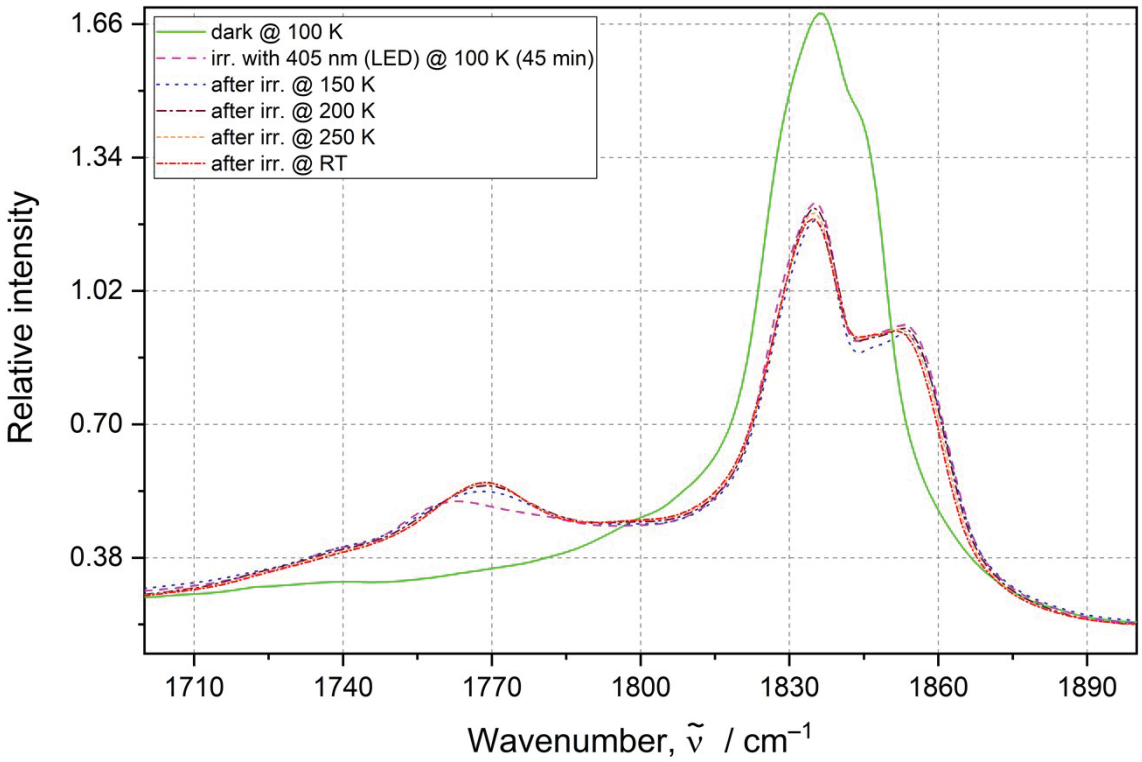

Figure S6 (continued). IR spectra collected at with no irradiation (green solid line) at 100 K, after irradiation with the 420 nm LED for 45 min. at 100 K (violet dashed line), and during temperature increasing: at 150 K (blue dotted line), at 200 K (brown dashed-dotted line), at 250 K (orange short dotted line) and at RT (red short dotted-dashed line).

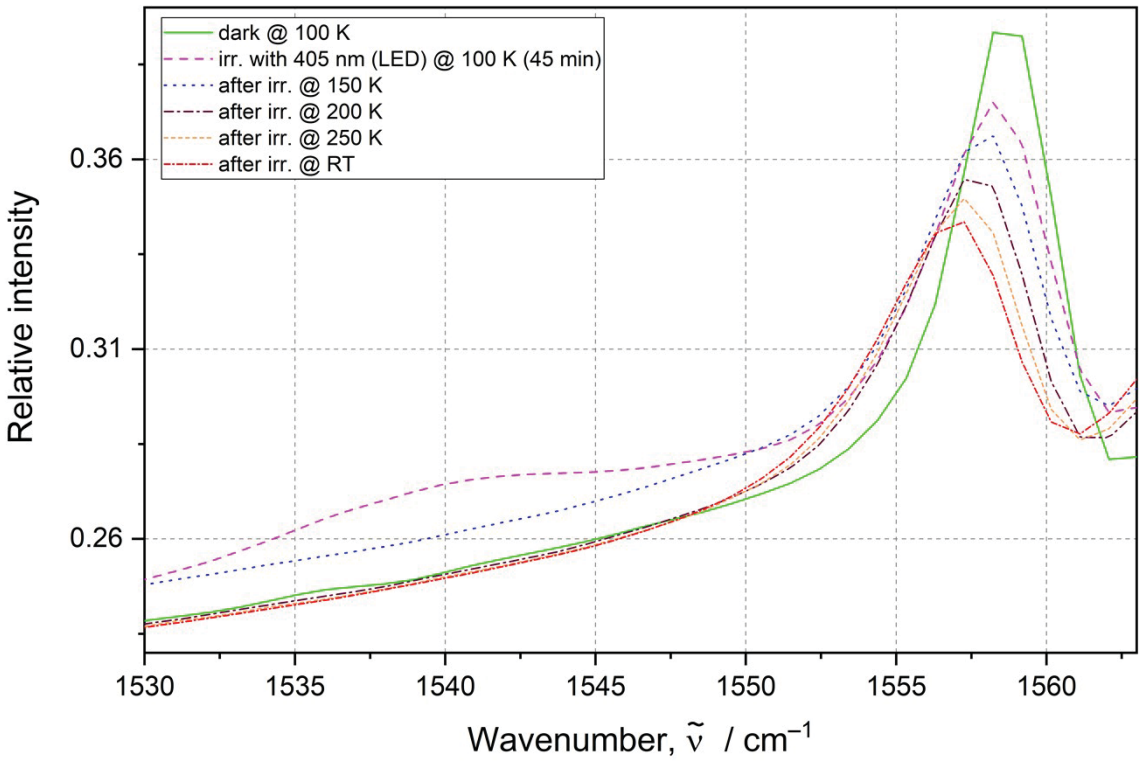

Figure S6 (continued). IR spectra collected at with no irradiation (green solid line) at 100 K, after irradiation with the 420 nm LED for 45 min. at 100 K (violet dashed line), and during temperature increasing: at 150 K (blue dotted line), at 200 K (brown dashed-dotted line), at 250 K (orange short dotted line) and at RT (red short dotted-dashed line).

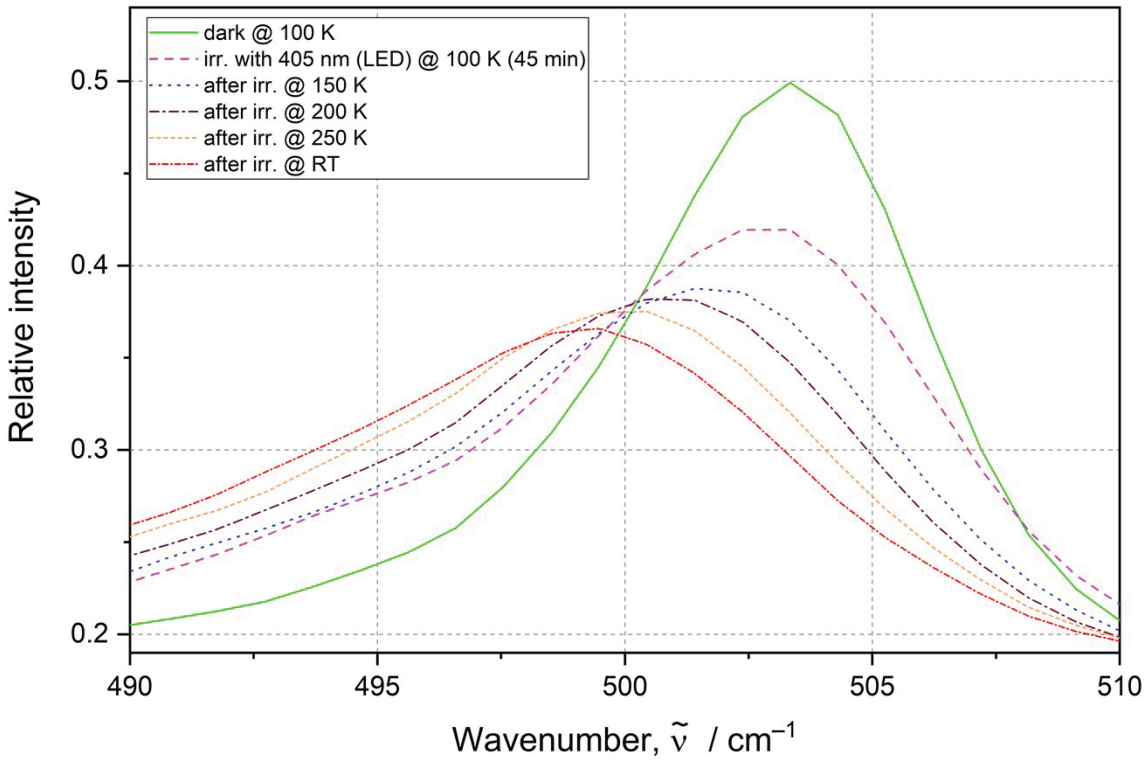

Figure S6 (continued). IR spectra collected at with no irradiation (green solid line) at 100 K, after irradiation with the 420 nm LED for 45 min. at 100 K (violet dashed line), and during temperature increasing: at 150 K (blue dotted line), at 200 K (brown dashed-dotted line), at 250 K (orange short dotted line) and at RT (red short dotted-dashed line).

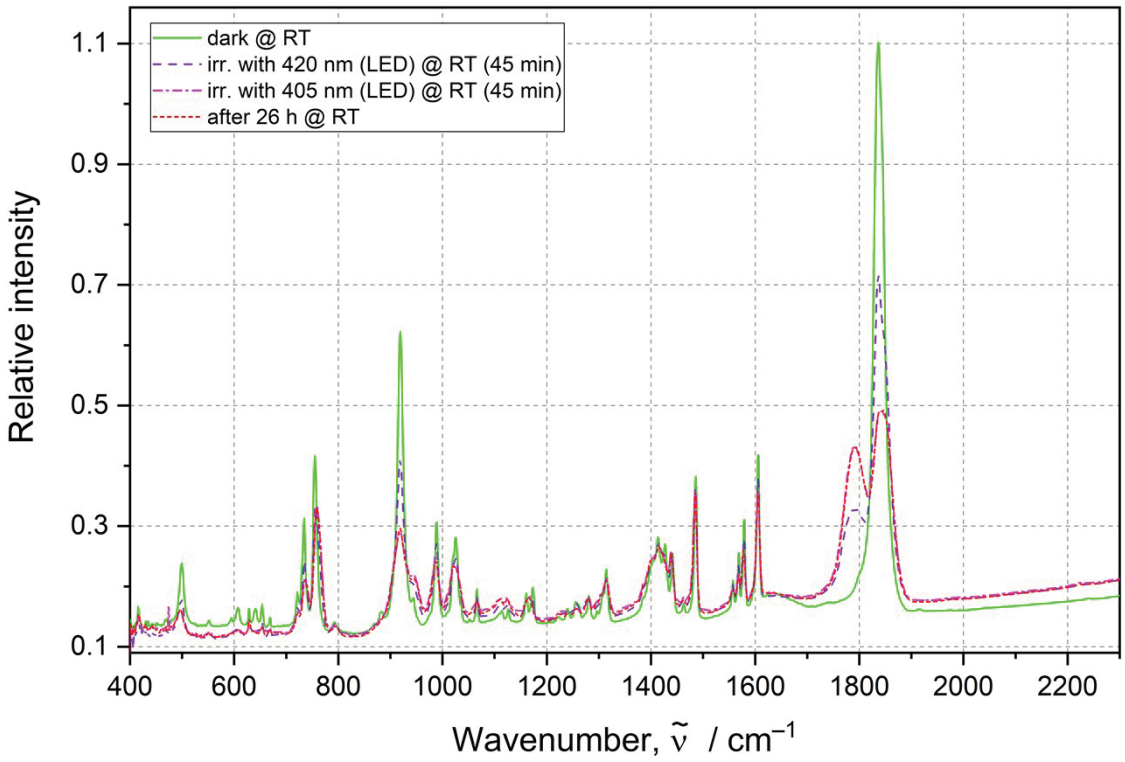

Figure S7. IR spectra collected at RT: no irradiation (green solid line), after irradiation with the 420 nm LED for 45 min. (violet dashed line), after irradiation with the 405 nm LED for 45 min. (magenta dashed-dotted line) and after subsequent waiting for 26 h (red short dashed line).

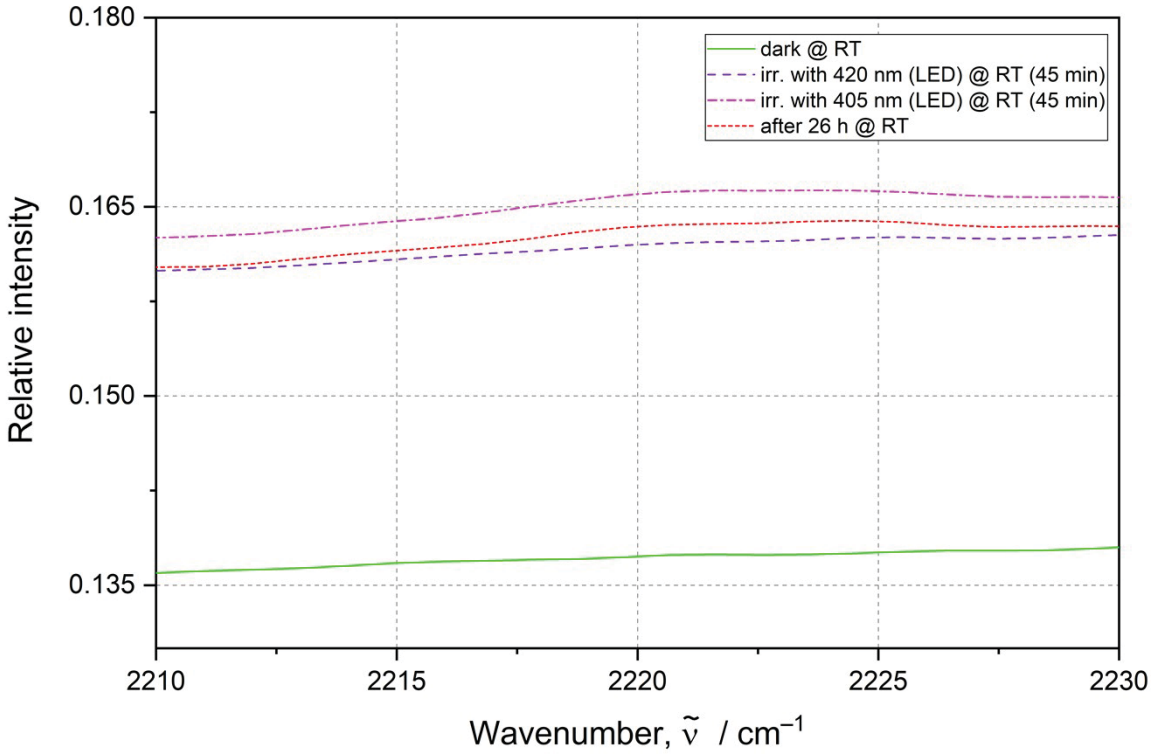

Figure S7 (continued). IR spectra collected at RT: no irradiation (green solid line), after irradiation with the 420 nm LED for 45 min. (violet dashed line), after irradiation with the 405 nm LED for 45 min. (magenta dashed-dotted line) and after subsequent waiting for 26 h (red short dashed line).

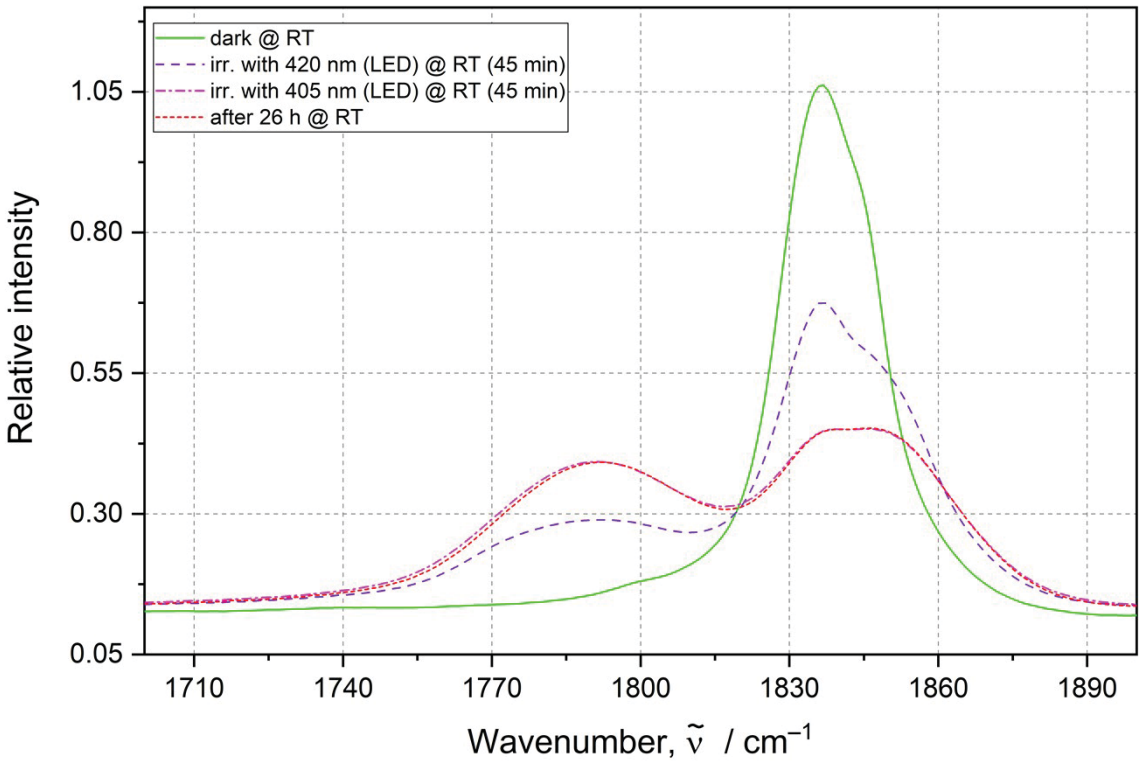

Figure S7 (continued). IR spectra collected at RT: no irradiation (green solid line), after irradiation with the 420 nm LED for 45 min. (violet dashed line), after irradiation with the 405 nm LED for 45 min. (magenta dashed-dotted line) and after subsequent waiting for 26 h (red short dashed line).

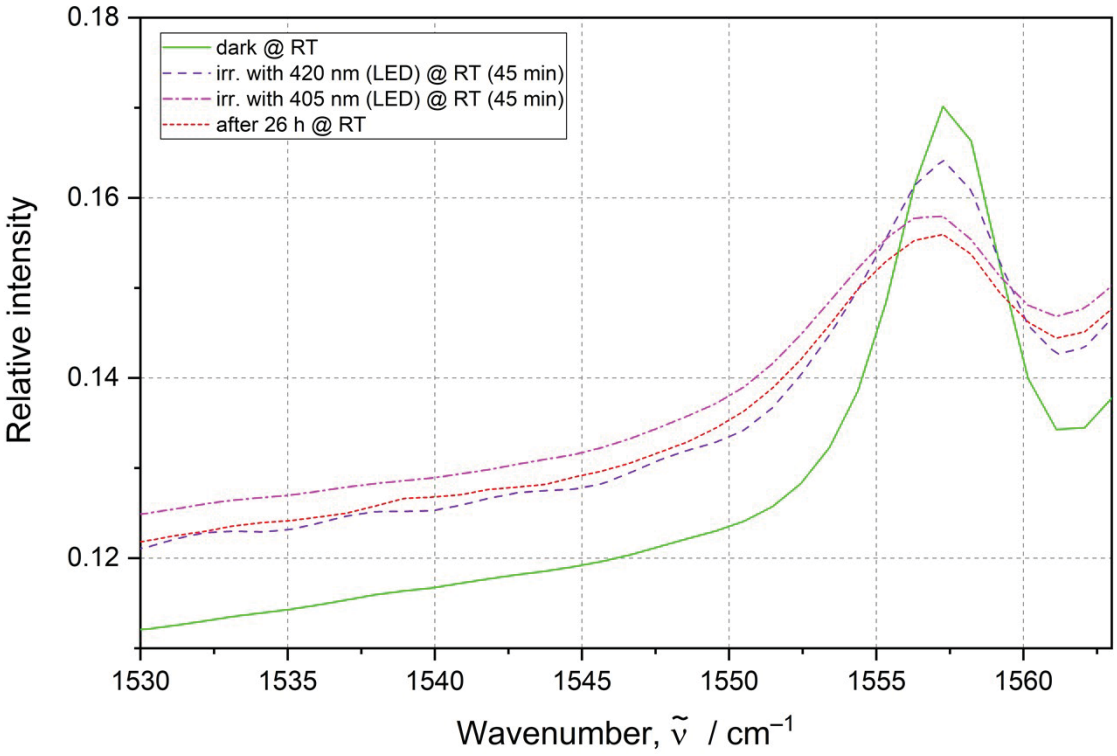

Figure S7 (continued). IR spectra collected at RT: no irradiation (green solid line), after irradiation with the 420 nm LED for 45 min. (violet dashed line), after irradiation with the 405 nm LED for 45 min. (magenta dashed-dotted line) and after subsequent waiting for 26 h (red short dashed line).

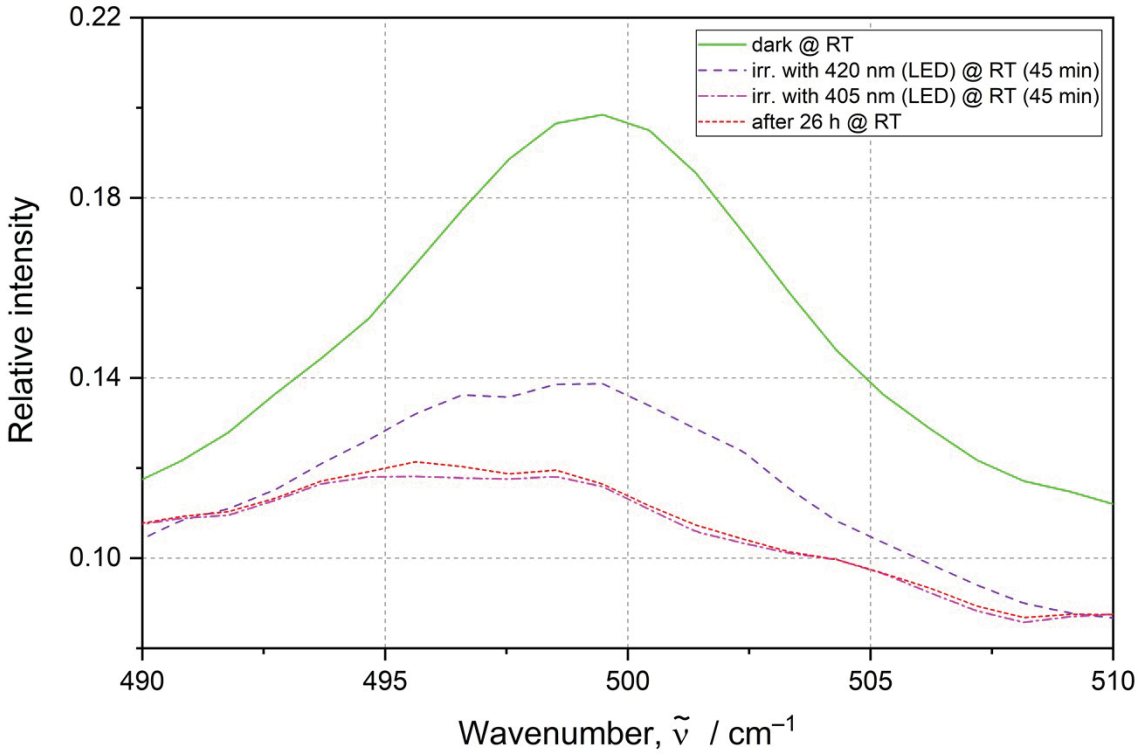

Figure S7 (continued). IR spectra collected at RT: no irradiation (green solid line), after irradiation with the 420 nm LED for 45 min. (violet dashed line), after irradiation with the 405 nm LED for 45 min. (magenta dashed-dotted line) and after subsequent waiting for 26 h (red short dashed line).

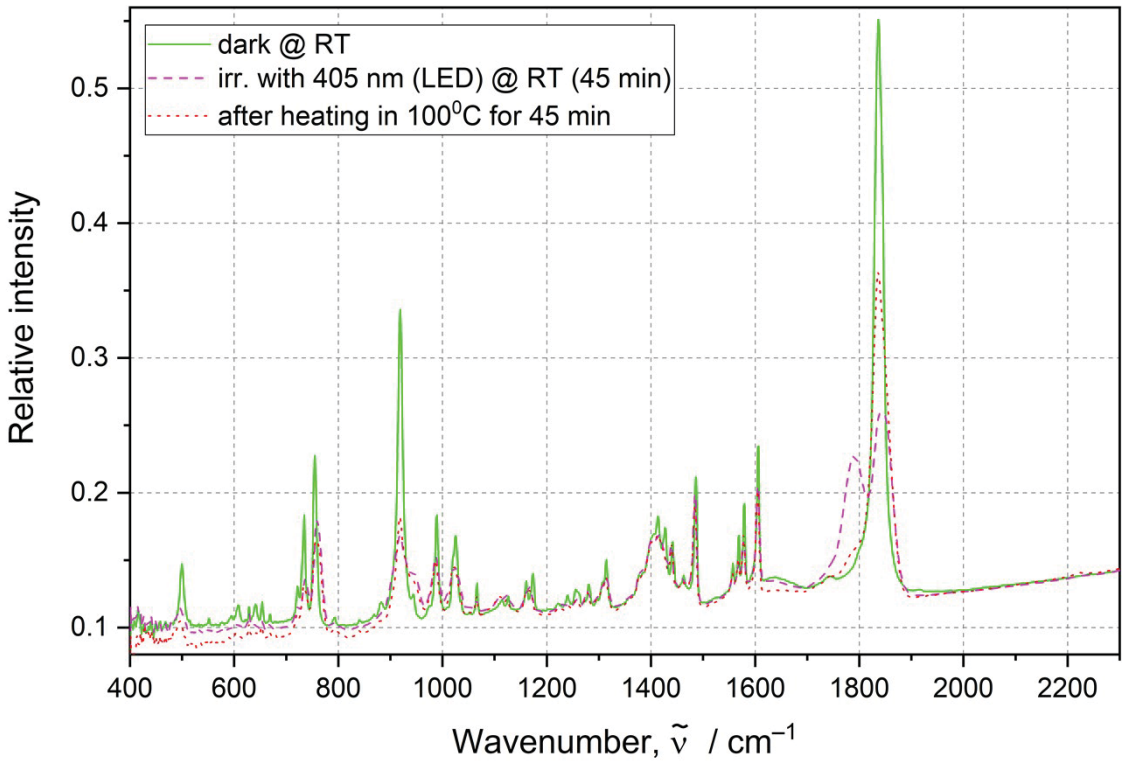

Figure S8. IR spectra collected at RT: no irradiation (green solid line), after irradiation with the 405 nm LED for 45 min. (magenta dashed line) and after heating in 100^{o}C for 45 minutes (red short dashed line).

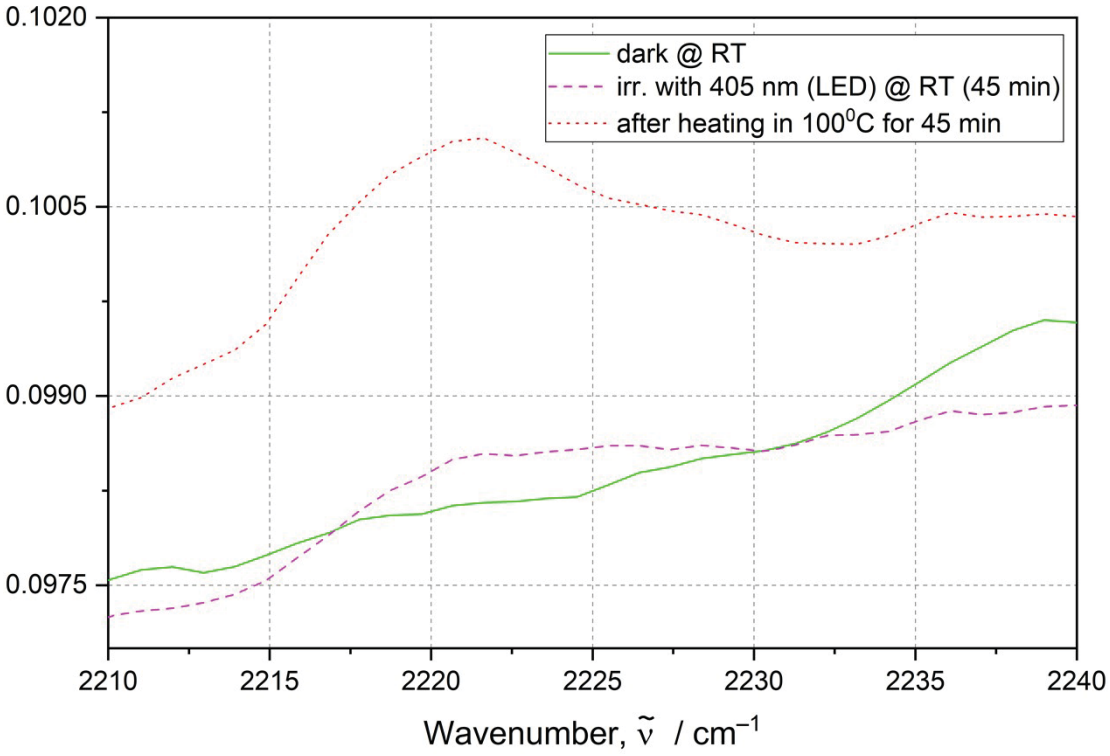

Figure S8 (continued). IR spectra collected at RT: no irradiation (green solid line), after irradiation with the 405 nm LED for 45 min. (magenta dashed line) and after heating in 100^{o}C for 45 minutes (red short dashed line).

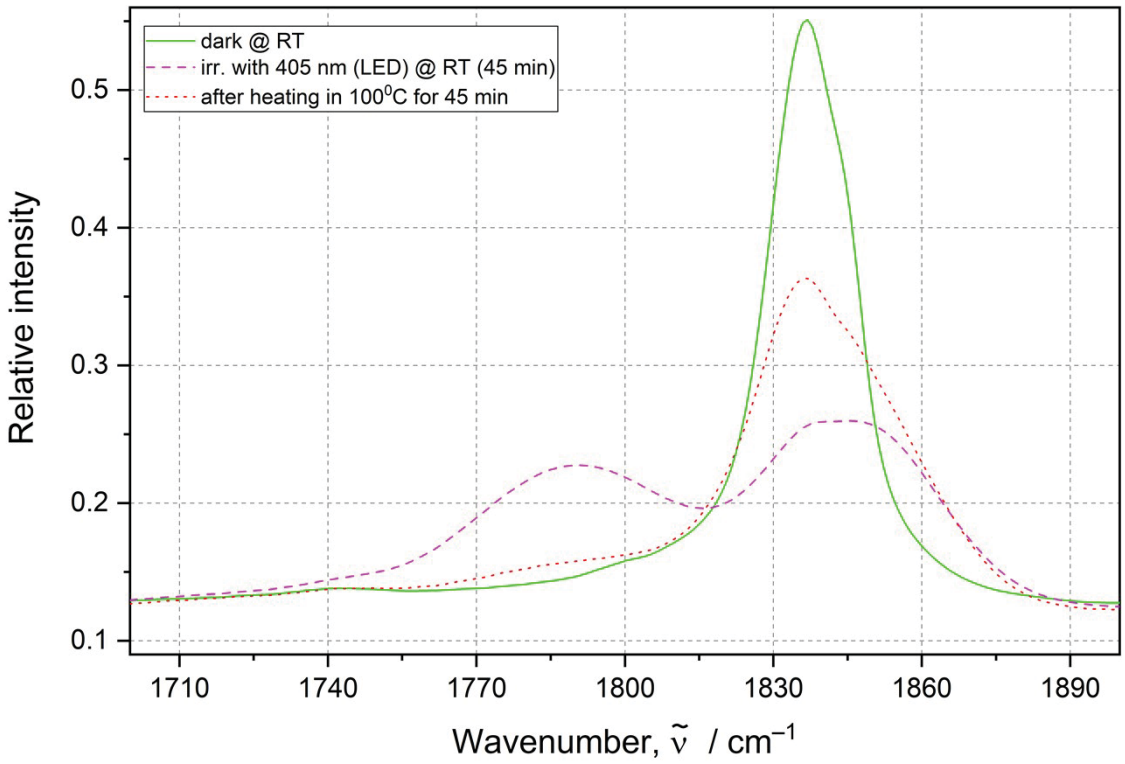

Figure S8 (continued). IR spectra collected at RT: no irradiation (green solid line), after irradiation with the 405 nm LED for 45 min. (magenta dashed line) and after heating in 100^{o}C for 45 minutes (red short dashed line).

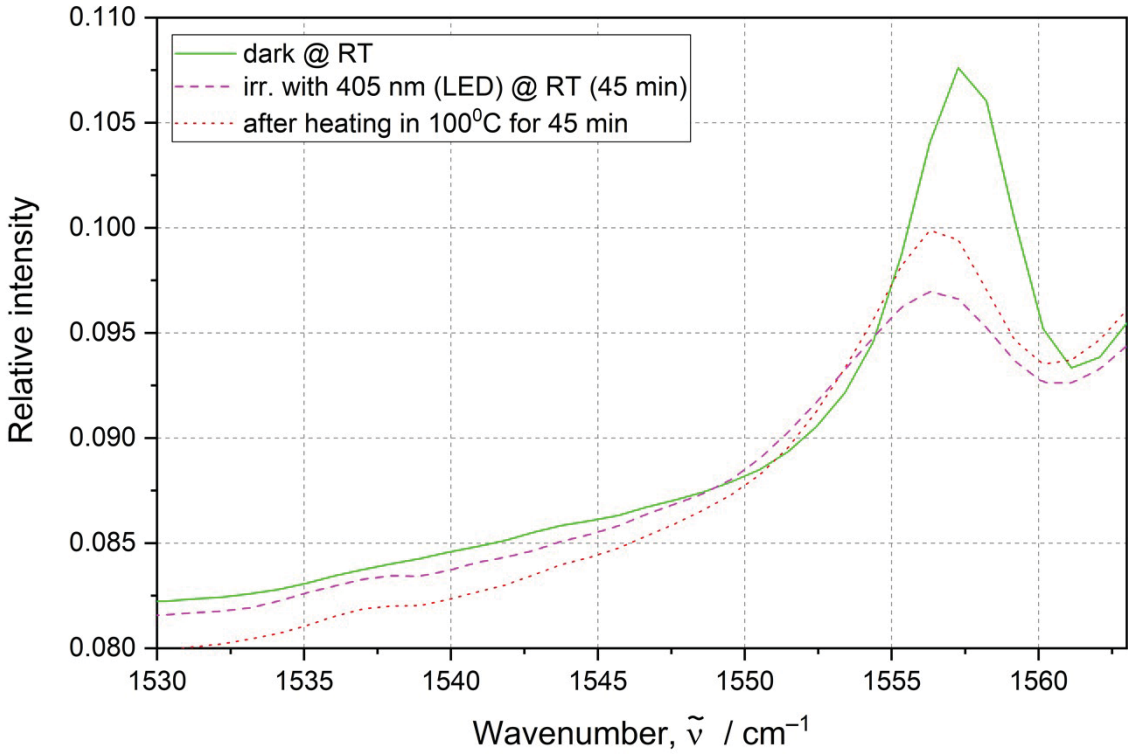

Figure S8 (continued). IR spectra collected at RT: no irradiation (green solid line), after irradiation with the 405 nm LED for 45 min. (magenta dashed line) and after heating in 100°C for 45 minutes (red short dashed line).

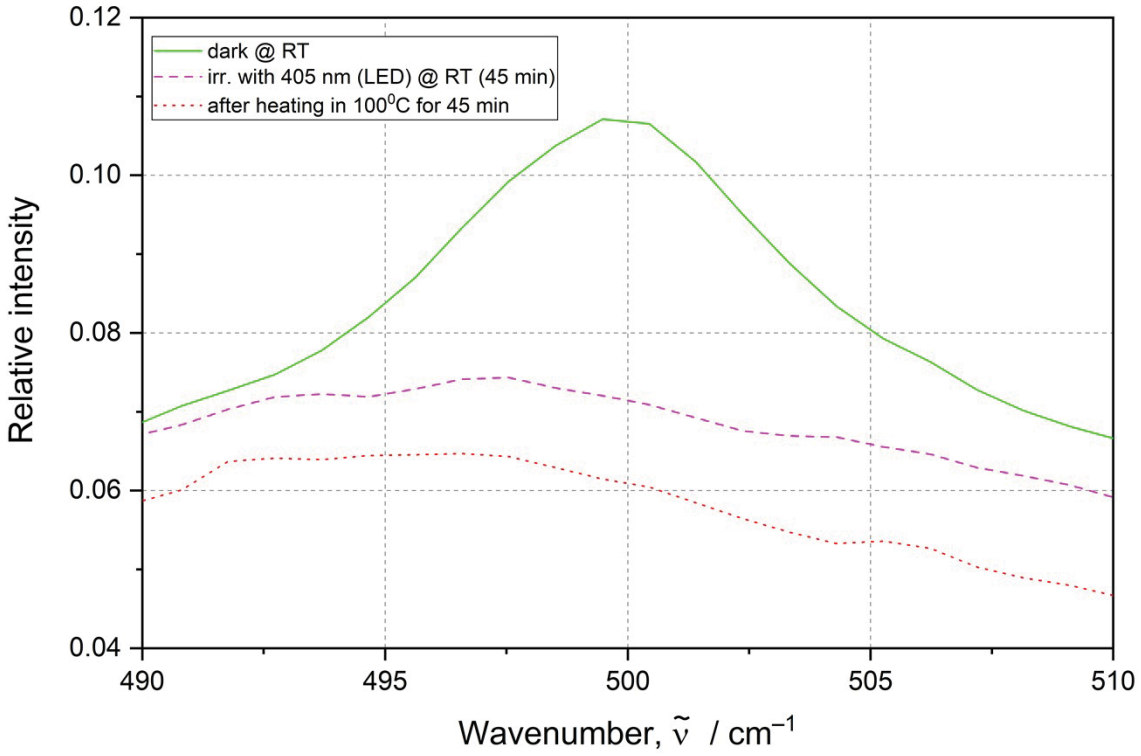

Figure S8 (continued). IR spectra collected at RT: no irradiation (green solid line), after irradiation with the 405 nm LED for 45 min. (magenta dashed line) and after heating in 100°C for 45 minutes (red short dashed line).

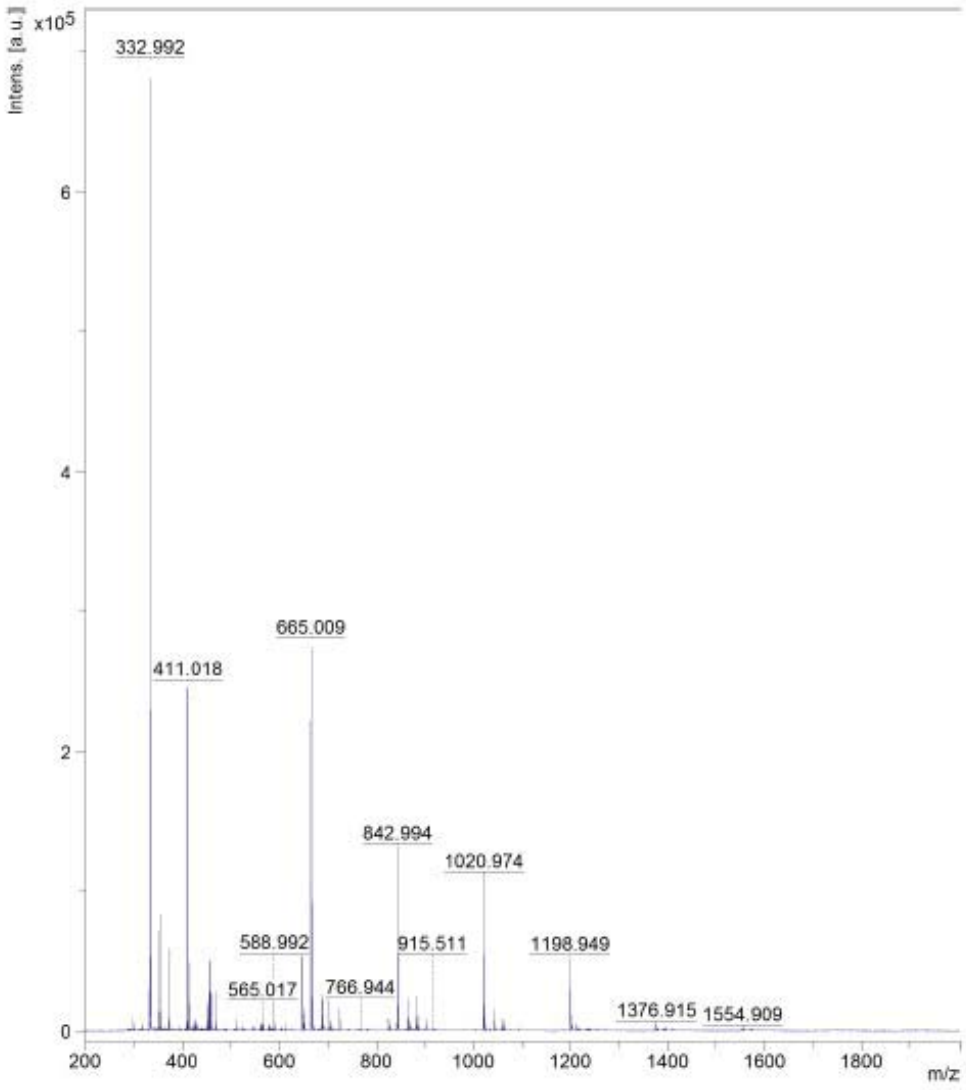

Figure S9. The MALDI-TOF-MS spectra of allyl alcohol oligomer.

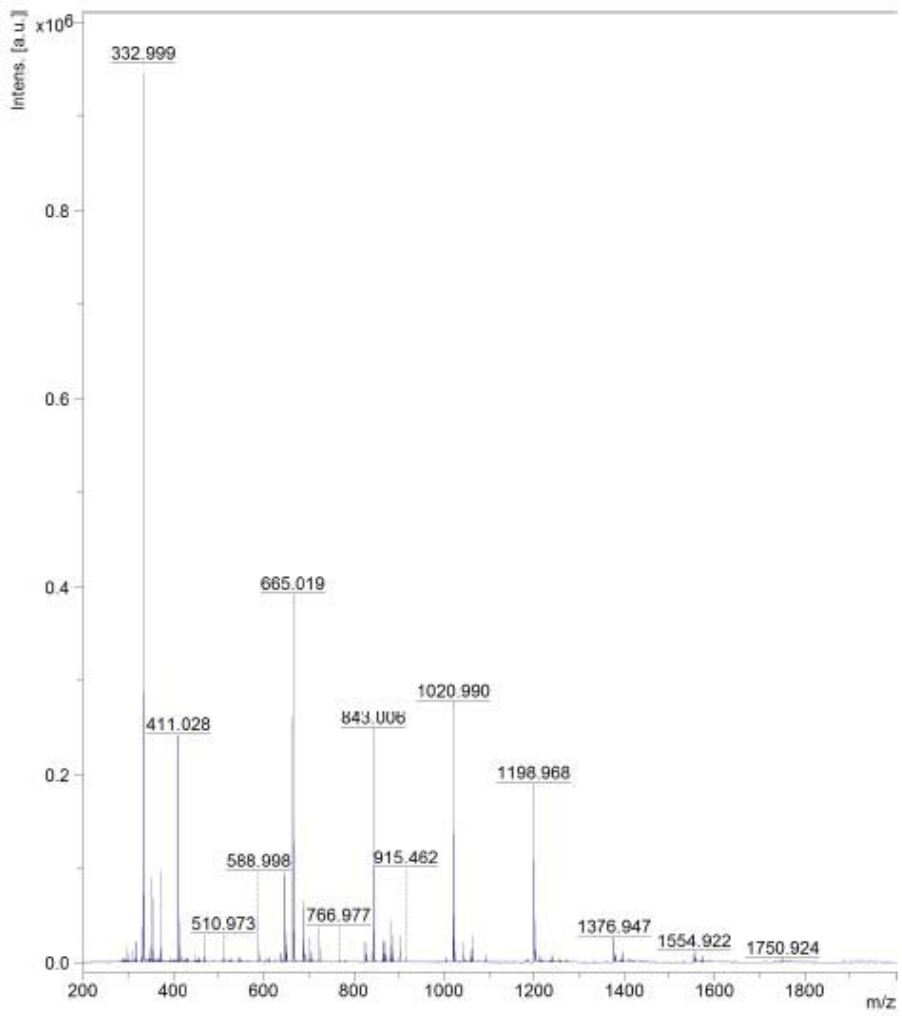

Figure S10. The MALDI-TOF-MS spectra of 2-chloro-2-propen-1-ol oligomer.

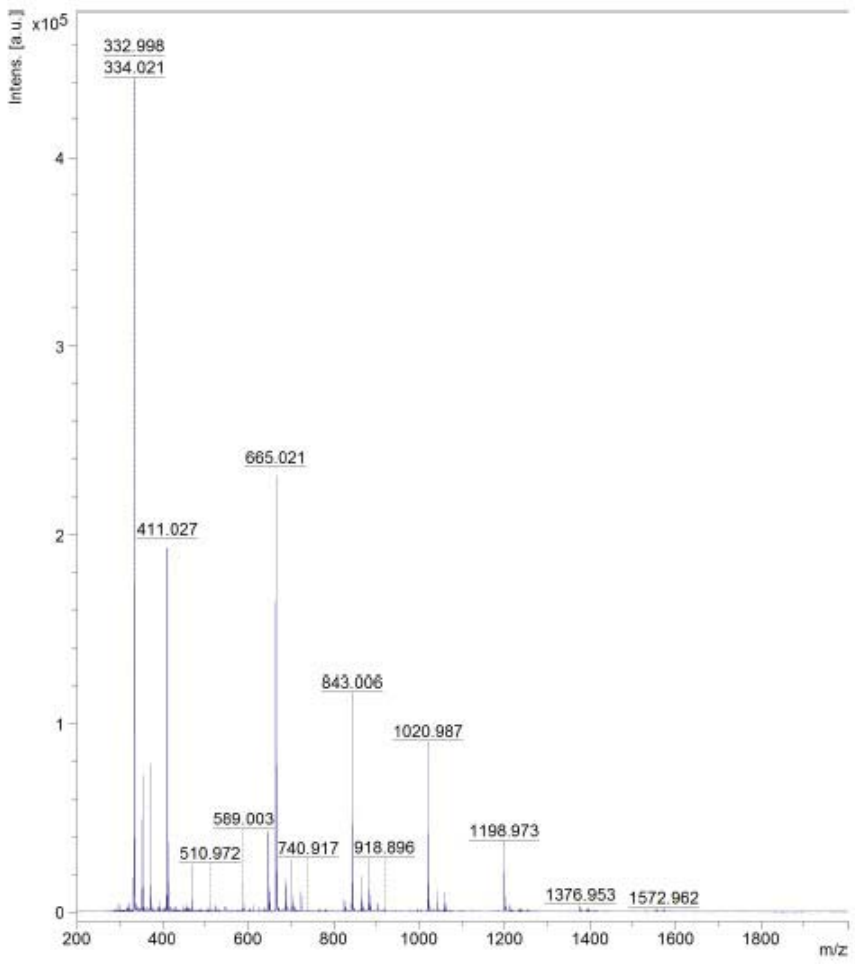

Figure S11. The MALDI-TOF-MS spectra of 3-buten-2-ol oligomer.

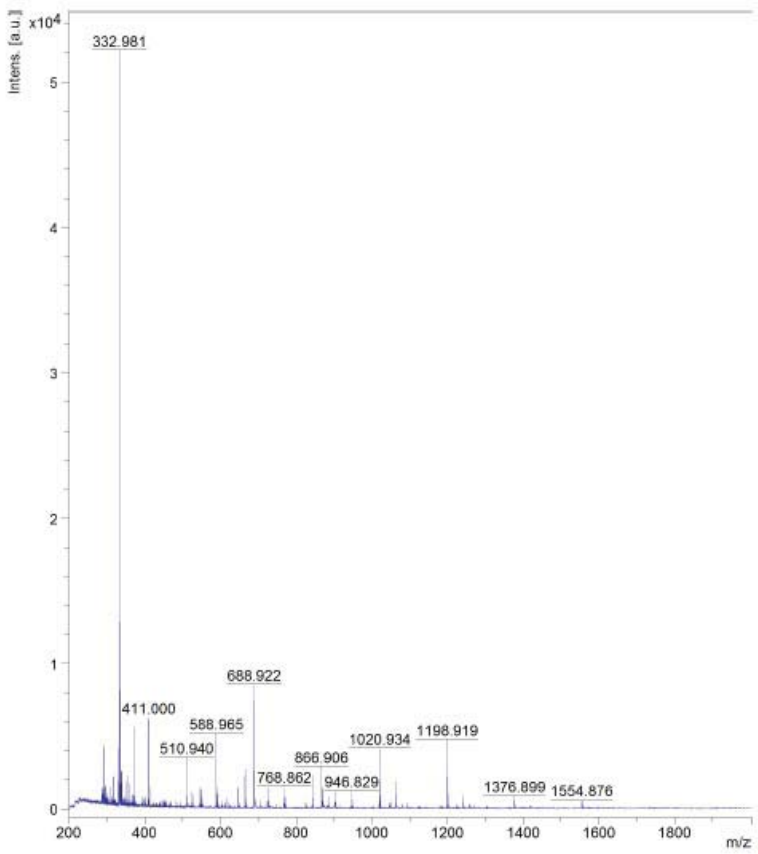

Figure S12. The MALDI-TOF-MS spectra of 2,3-dibormo-2-propen-1-ol oligomer.

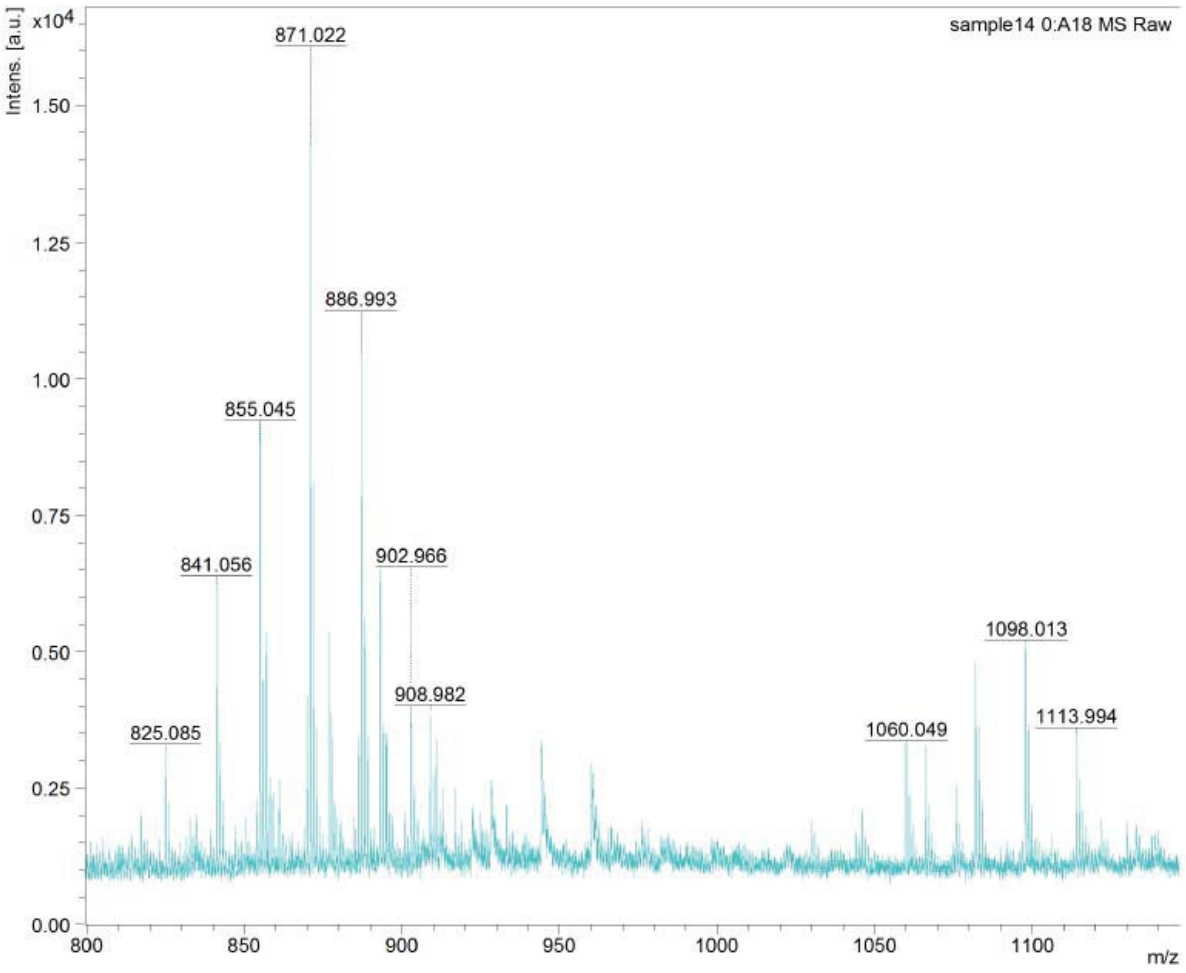

Figure S13. The MALDI-TOF-MS spectra of ethylene oligomer.

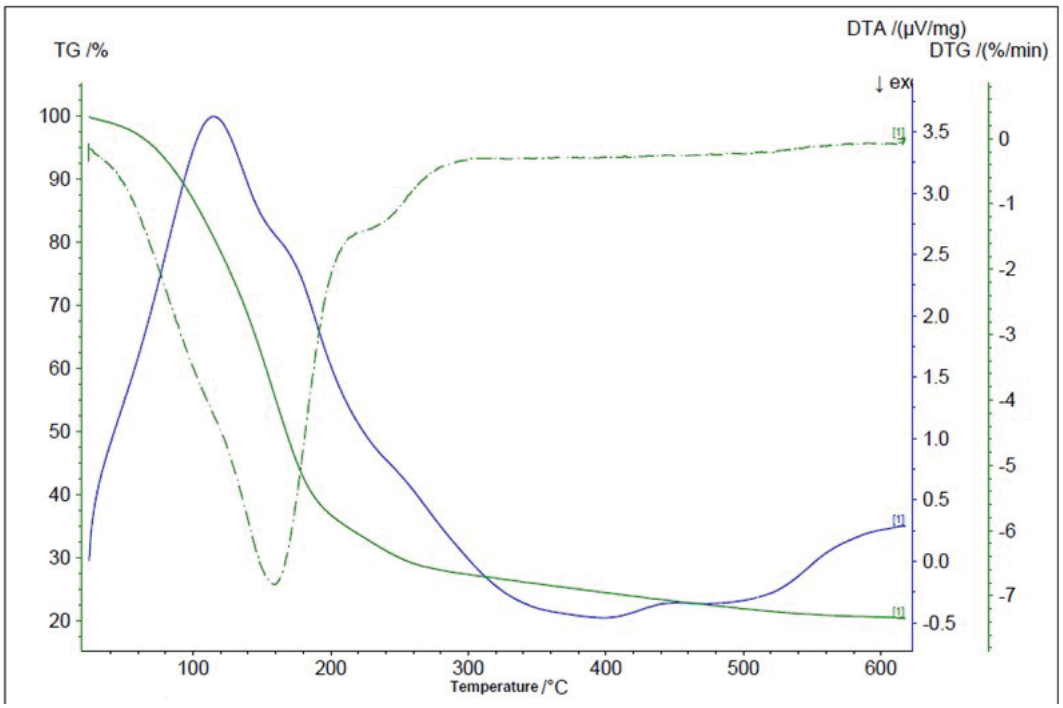

Figure S14. The TG and DTA curves for the allyl alcohol oligomer obtained using [Ru(2-phenylpyridine)$(Cl)_2$(DMSO)(NO)] as a precatalyst.

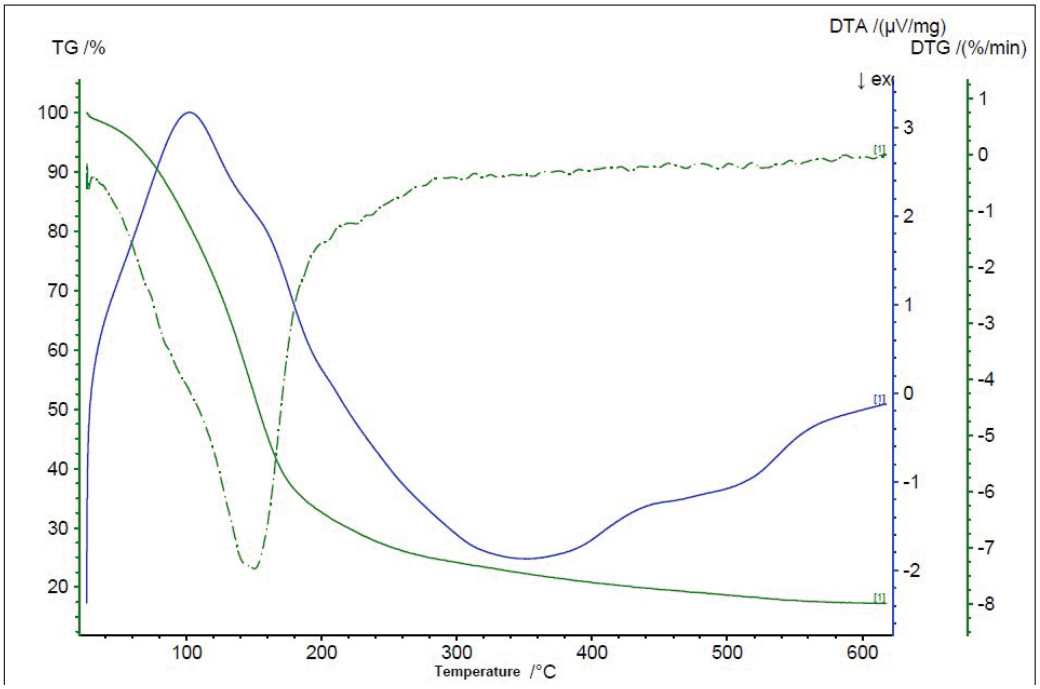

Figure S15. The TG and DTA curves for the 2-chloro-2-propen-1-ol oligomer obtained using [Ru(2-phenylpyridine)$(Cl)_2$(DMSO)(NO)] as a precatalyst.

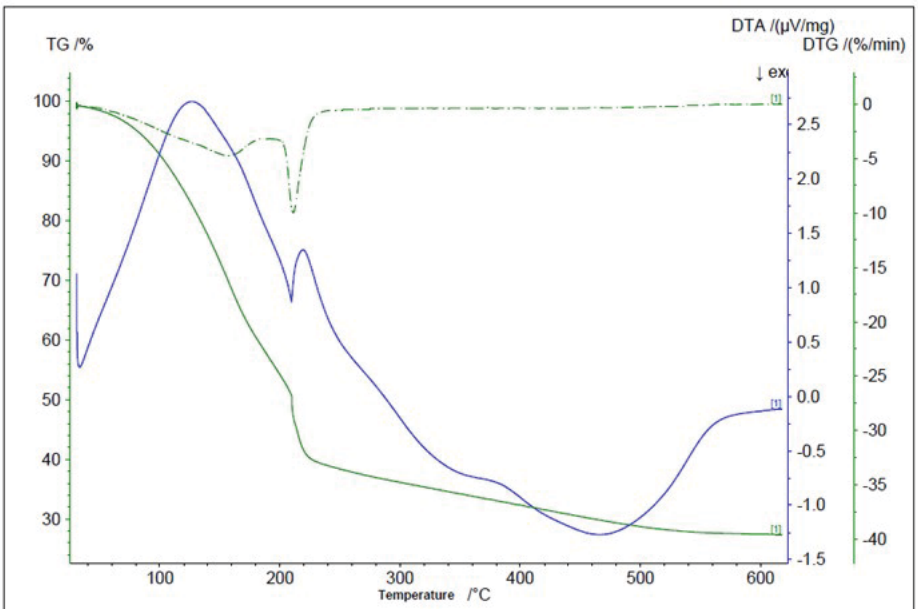

Figure S16. The TG and DTA curves for the 3-buten-2-ol oligomer obtained using [Ru(2-phenylpyridine)$(Cl)_2$(DMSO)(NO)] as a precatalyst.

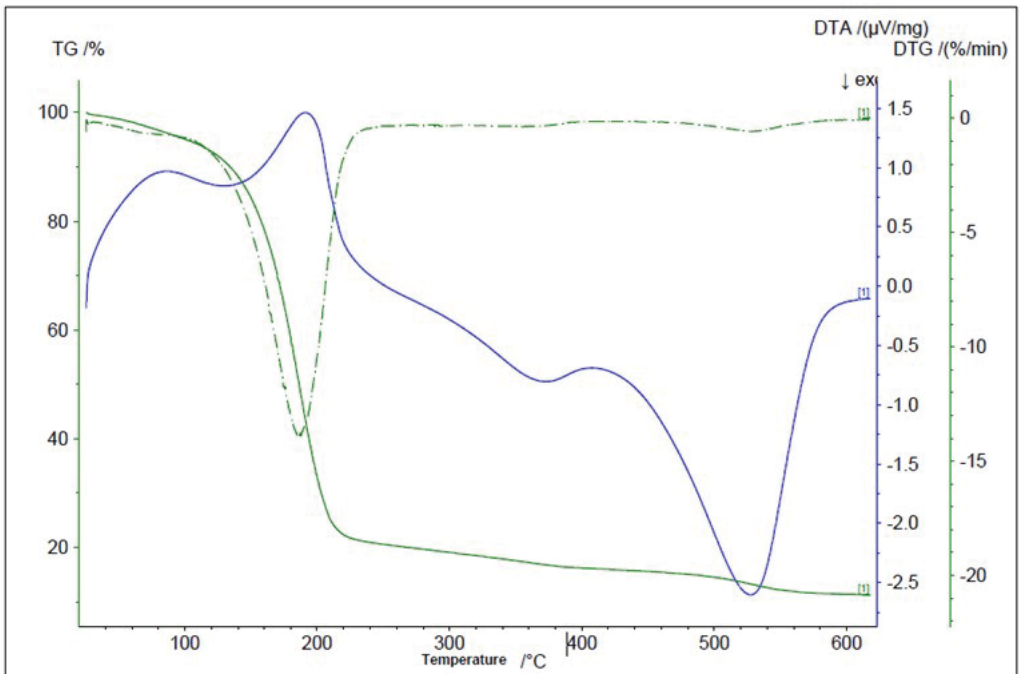

Figure S17. The TG and DTA curves for the 2,3-dibromo-2-propen-1ol oligomer obtained using [Ru(2-phenylpyridine)$(Cl)_2$(DMSO)(NO)] as a precatalyst.

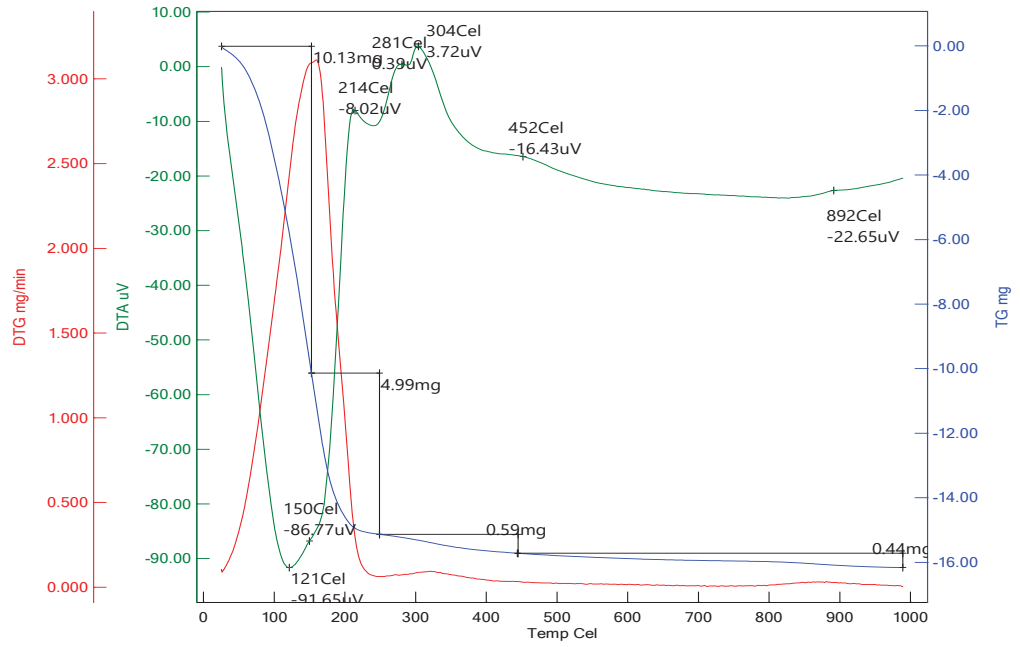

Figure S18. The TG and DTA curves for the ethylene oligomer obtained using [Ru(2-phenylpyridine)$(Cl)_2$(DMSO)(NO)] as a precatalyst.

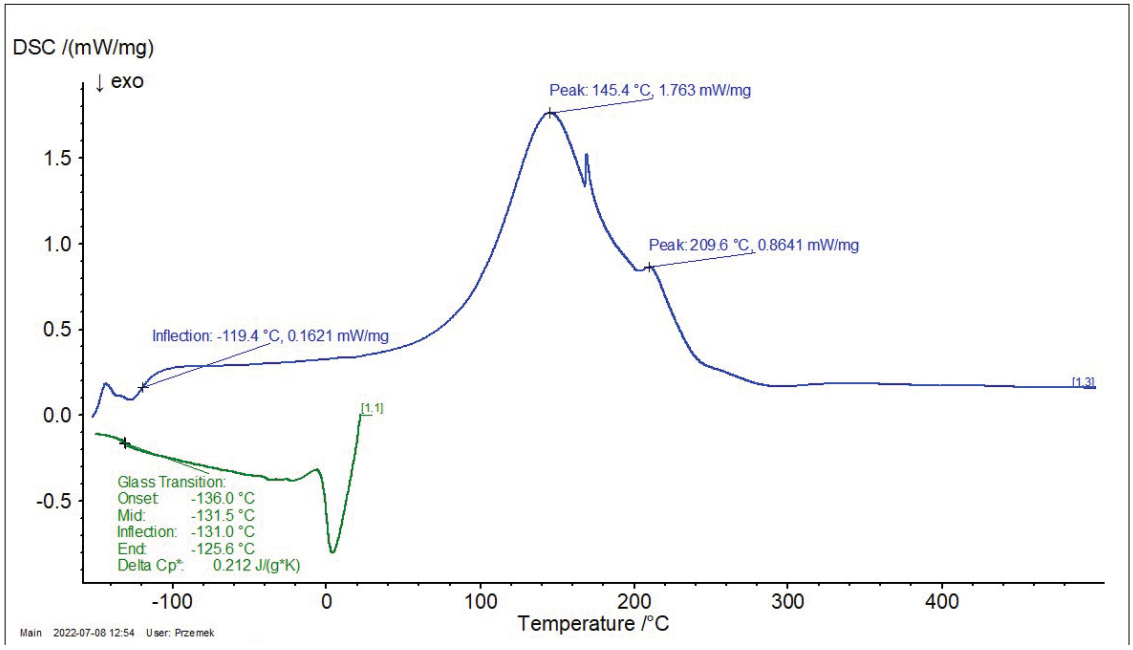

Figure S19. The DSC curve of allyl alcohol oligomer obtained using [Ru(2-phenylpyridine)$(Cl)_2$(DMSO)(NO)] as a precatalyst.

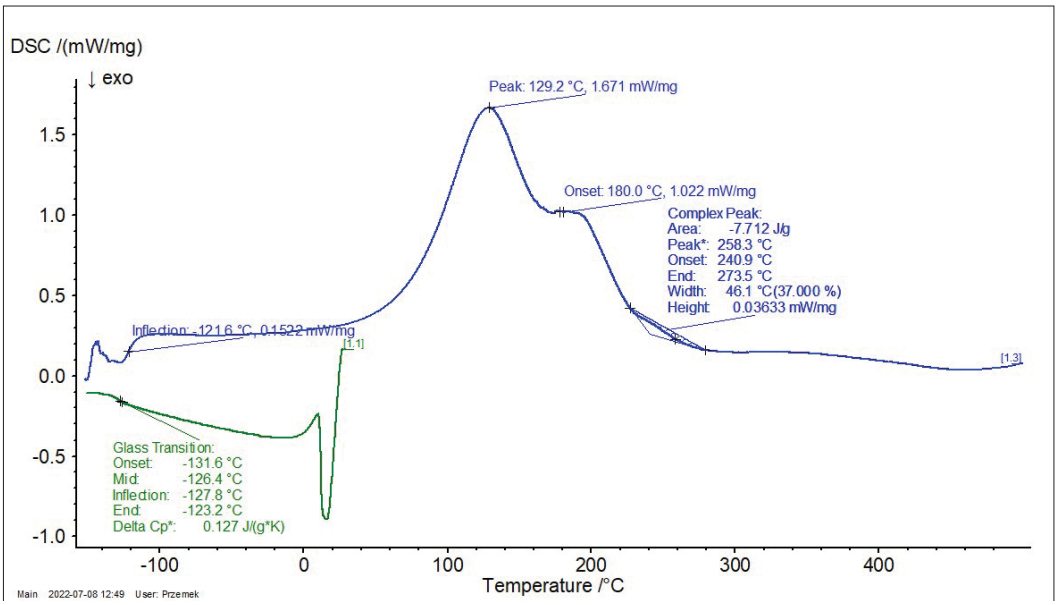

Figure S20. The DSC curve of 2-chloro-2-propen-1-ol oligomer obtained using [Ru(2-phenylpyridine)$(Cl)_2$(DMSO)(NO)] as a precatalyst.

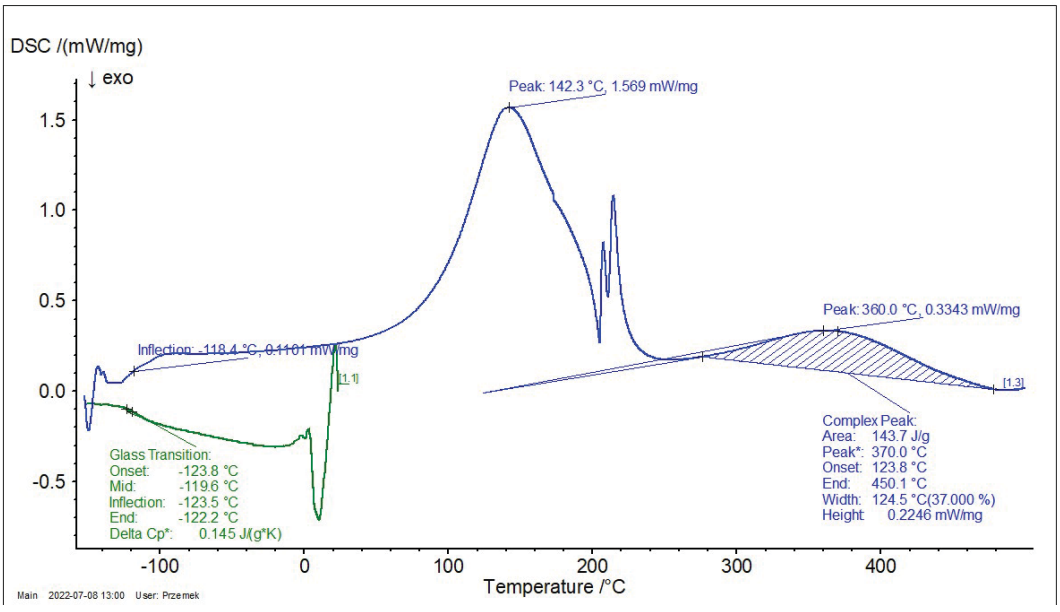

Figure S21. The DSC spectra of 3-buten-2-ol oligomer obtained using [Ru(2-phenylpyridine)$(Cl)_2$(DMSO)(NO)] as a precatalyst.

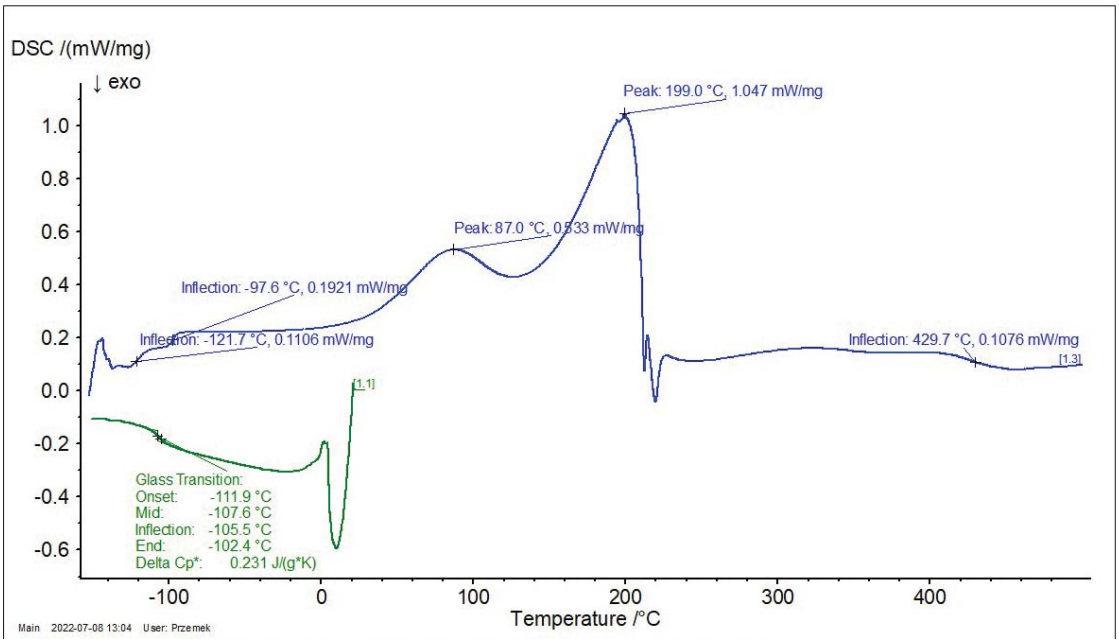

Figure S22. The DSC spectra of 2,3-dibromo-2-propen-1-ol oligomer obtained using [Ru(2-phenylpyridine)$(Cl)_2$(DMSO)(NO)] as a precatalyst.

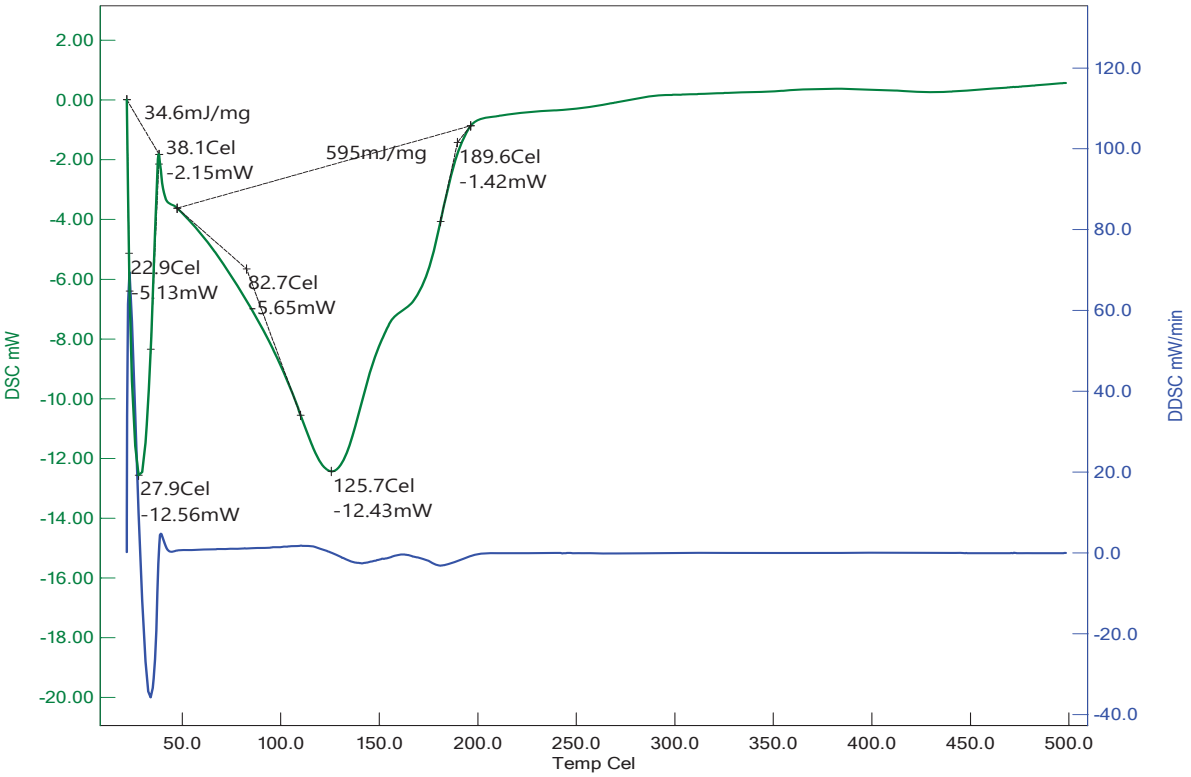

Figure S23. The DSC spectra of ethylene oligomer obtained using [Ru(2-phenylpyridine)$(Cl)_2$(DMSO)(NO)] as a precatalyst.

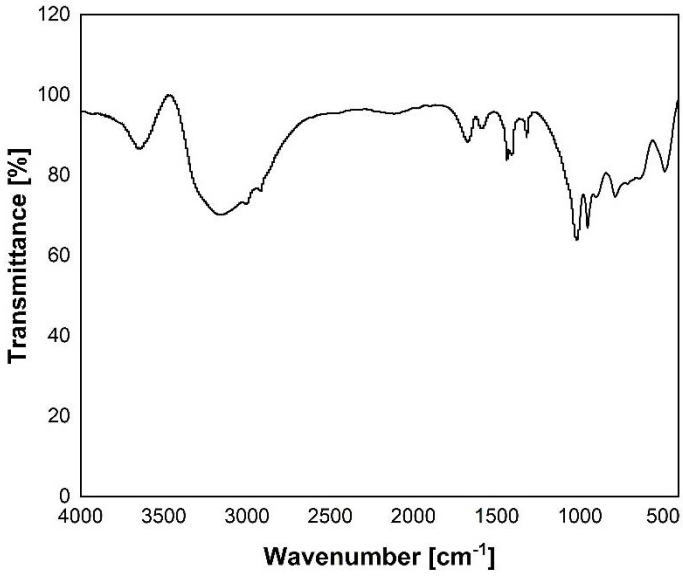

Figure S24. The FTIR spectrum of the allyl alcohol oligomer obtained using [Ru(2-phenylpyridine)$(Cl)_2$(DMSO)(NO)] as a precatalyst.

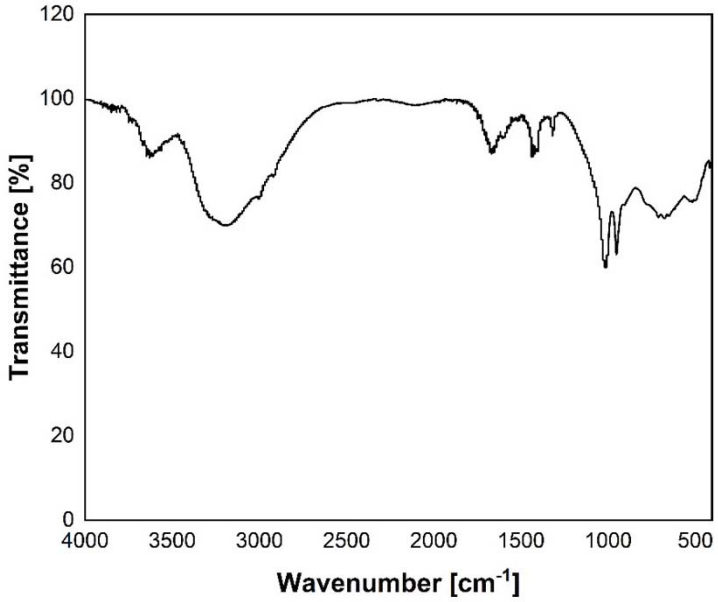

Figure S25. The FTIR spectrum of the 2-chloro-2-propen-1-ol oligomer obtained using [Ru(2-phenylpyridine)$(Cl)_2$(DMSO)(NO)] as a precatalyst.

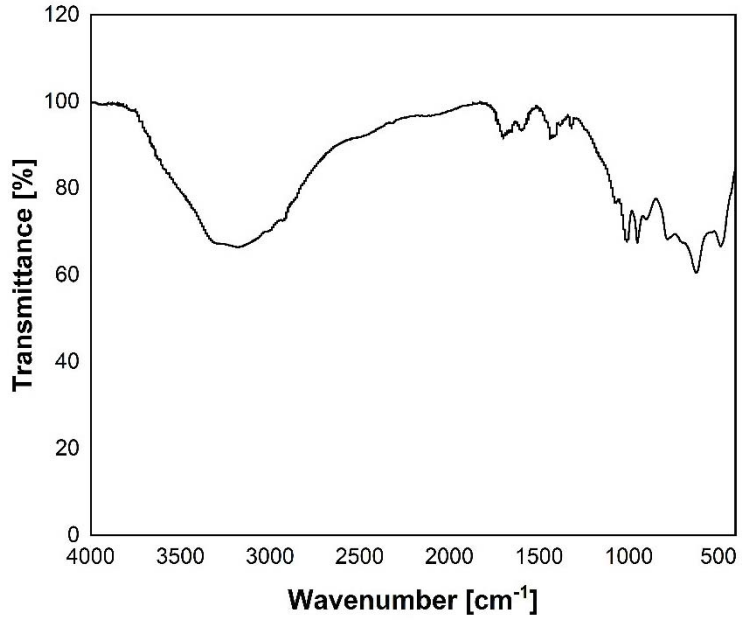

Figure S26. The FTIR spectrum of the 3-buten-2-ol oligomer obtained using [Ru(2-phenylpyridine)$(Cl)_2$(DMSO)(NO)] as a precatalyst.

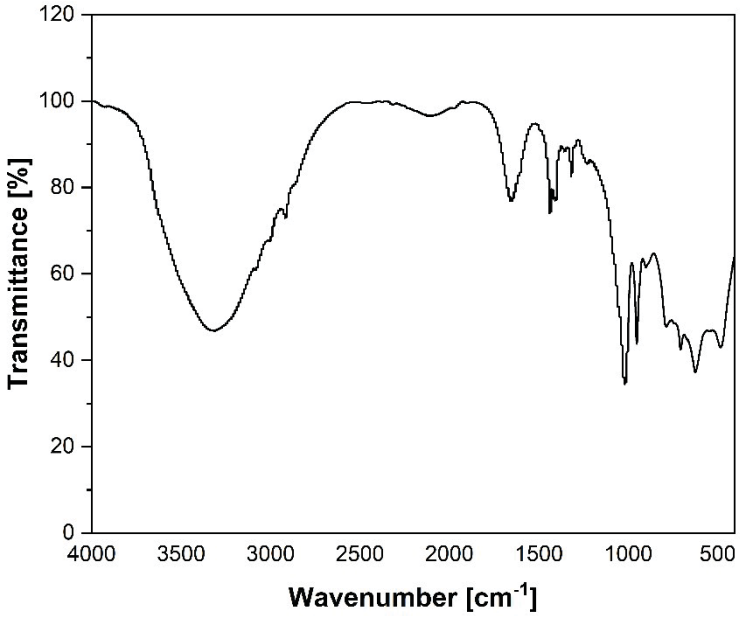

Figure S27. The FTIR spectrum of the 2,3-dibromo-2-propen-1-ol oligomer obtained using [Ru(2-phenylpyridine)$(Cl)_2$(DMSO)(NO)] as a precatalyst.

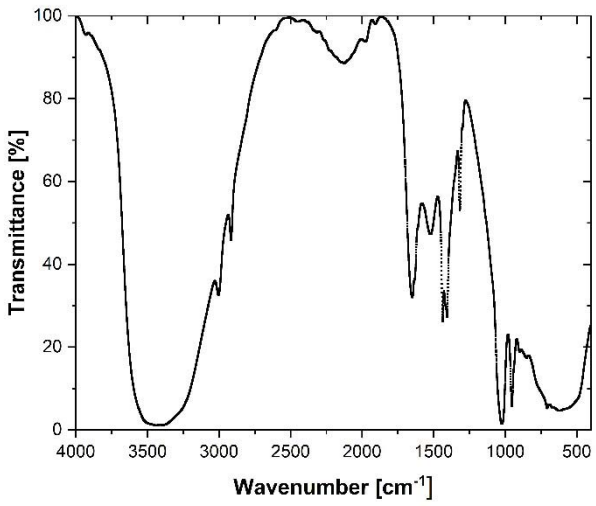

Figure S28. The FTIR spectrum of the ethylene oligomer obtained using [Ru(2-phenylpyridine)$(Cl)_2$(DMSO)(NO)] as a precatalyst.

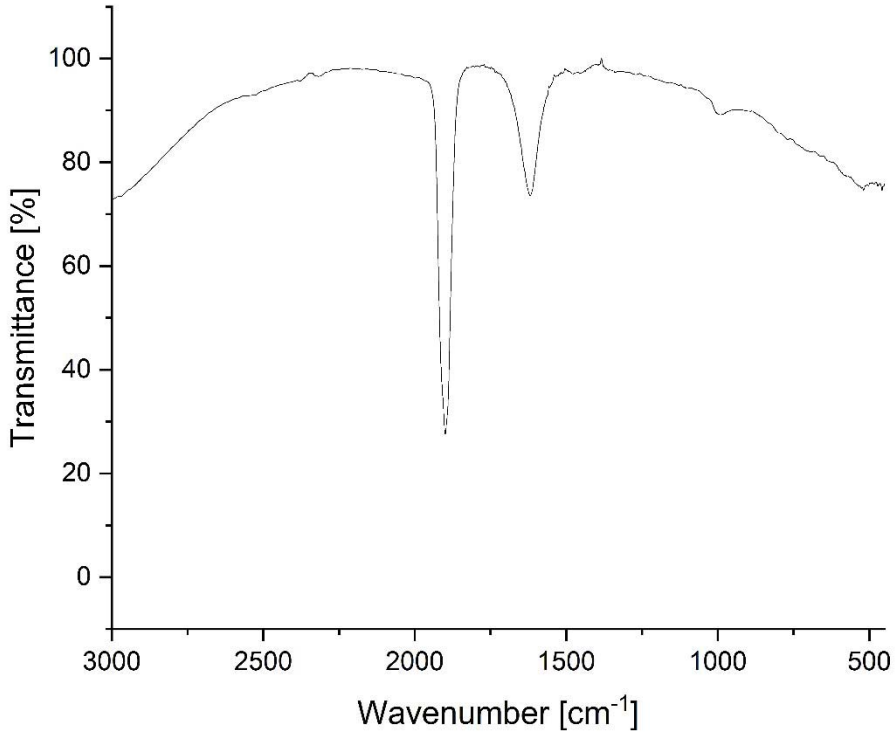

Figure S29. The FTIR spectrum of the $RuCl_3NO$ salt from BDH.

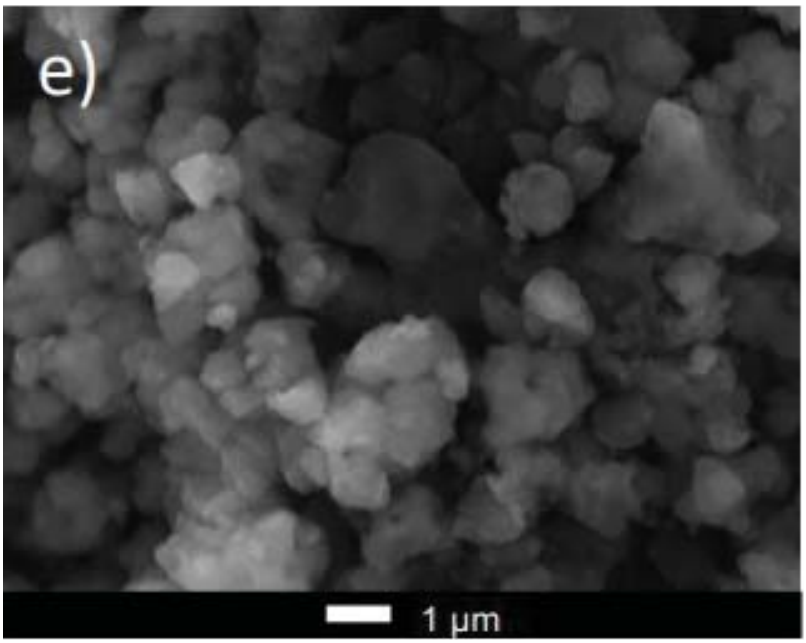

Figure S30. SEM image of the ethylene oligomer.

Table S2. Optimization of the oligomerization process of selected monomers

Monomer	Activator	Ru(III):Al	t (℃)	p (bar)	C_a[a]
		1:500	30		159.2
Allyl alcohol	MAO				
		1:1000			268.7
		1:1500			283.6
		1:2000			185.1
		1:2500			69.65
		1:1500	50		258.2
		1:1500	70		318.4
Ethylene		1:1500	30	0.3	754.7
		1:1500		0.5	755.6
		1:1500		0.8	209.7
		1:1500	50	0.5	576.5
		1:1500	70		130.5

[a]($g \bullet mmol^{-1} \bullet h^{-1} \bullet bar^{-1}$)

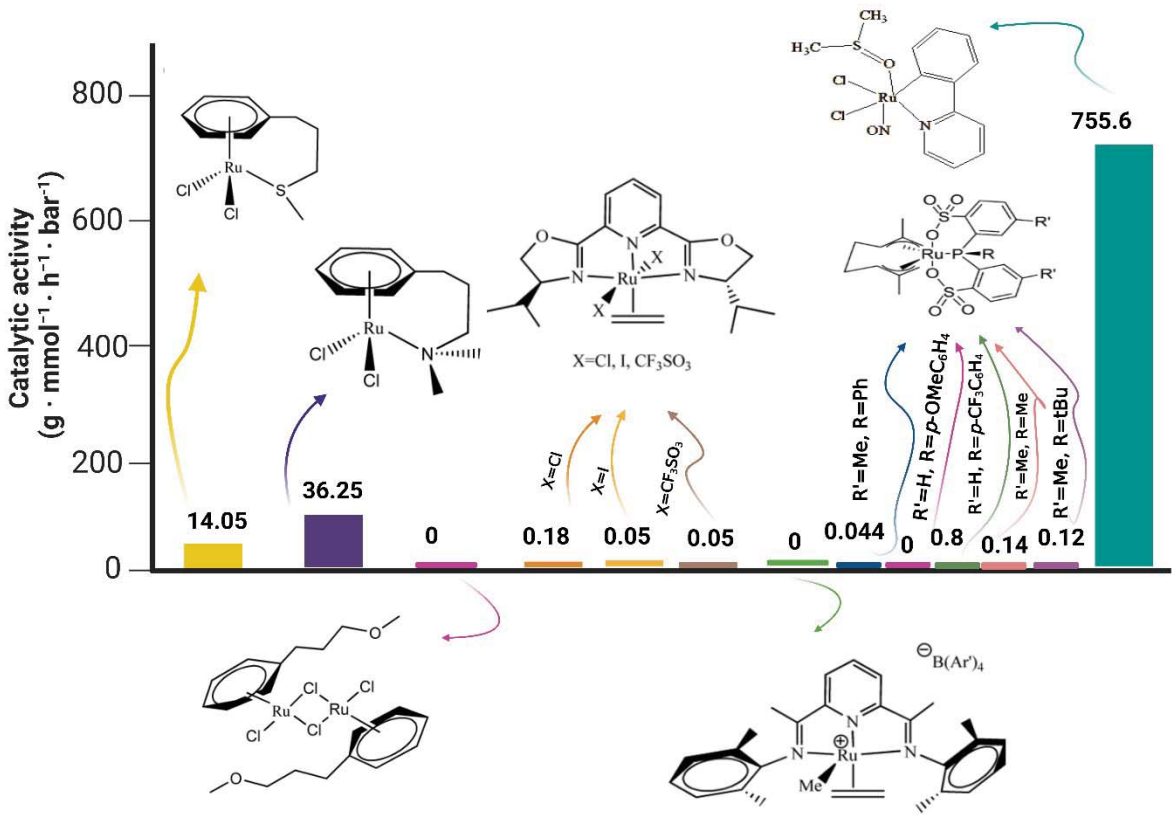

Figure S31. Comparison of the catalytic properties of ruthenium(II/III/IV) precatalysts in the oligomerization and polymerization of ethylene [21–24]. Created with BioRender.com

Proposed mechanism of coordination polymerization based on the literature.

In homogeneous catalysis, the role of MAO (methylaluminoxane) is to alkylate the precatalyst because of the exchange of ligands. The consequence is the formation of a metal-alkyl complex (Fig. S32). Then, the chloride anion is probably replaced, which correlates with the formation of the polymerization active center - the ruthenium(III) cation and the MAO anion (activation). The weakly coordinating methylaluminoxane protects the active center, so despite the small steric hindrance due to the ligands, i.e. NO and DMSO, the active center of ruthenium is not immediately poisoned. In the initiation stage, a bond is formed between the ruthenium ion and a monomer molecule, e.g. ethylene (metal-carbon bond). According to the Arlam and Cossee mechanism[25,26], propagation occurs (monomer coordination and insertion). In turn, the termination involves the elimination of β-H (or transfer to the monomer)[27–30].

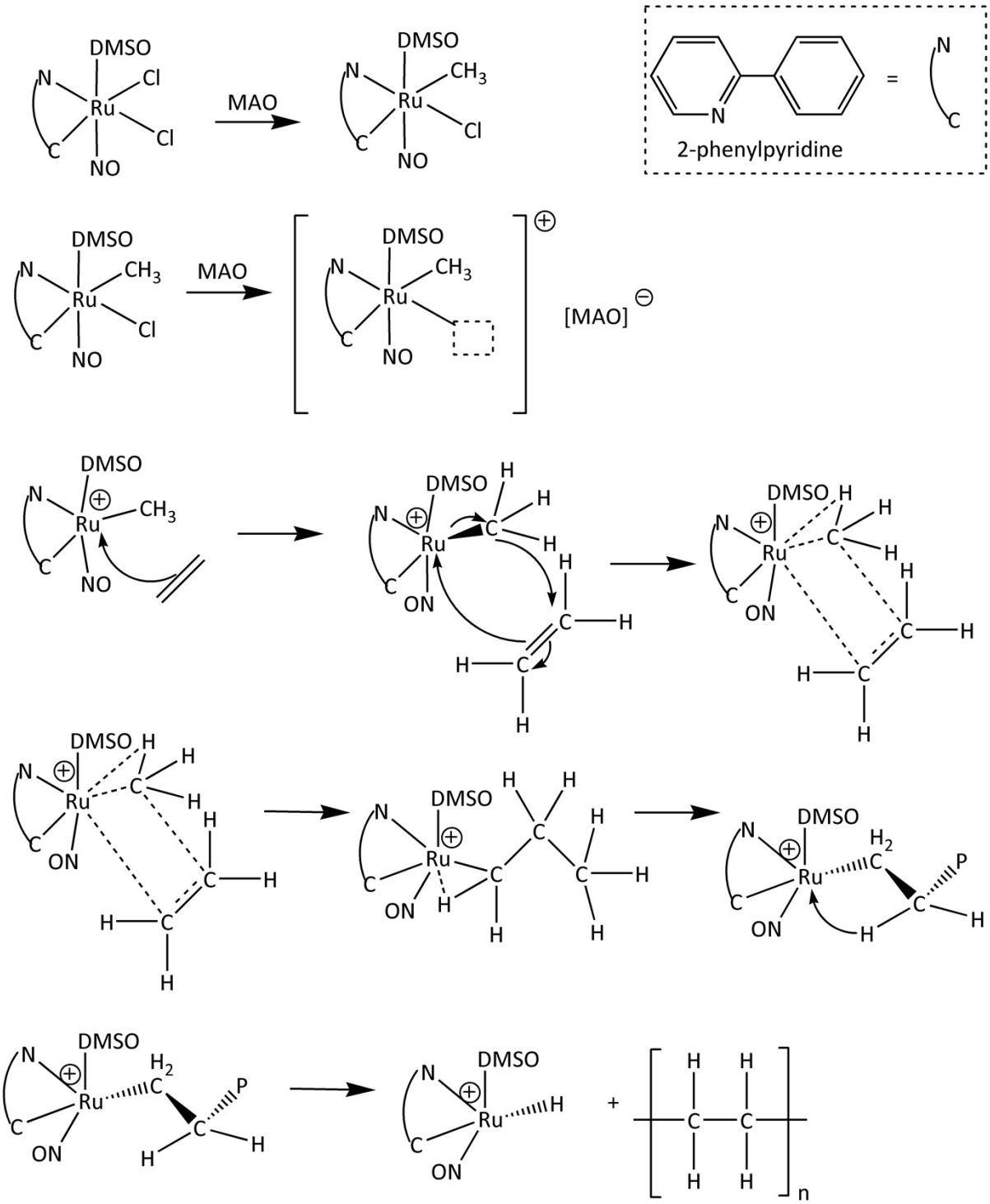

Figure S32. Proposed mechanism of coordination polymerization of ethylene using **Ru1** as a precatalyst and MAO as an activator (P = polymer and NC = 2-phenylpyridine)[25–30].

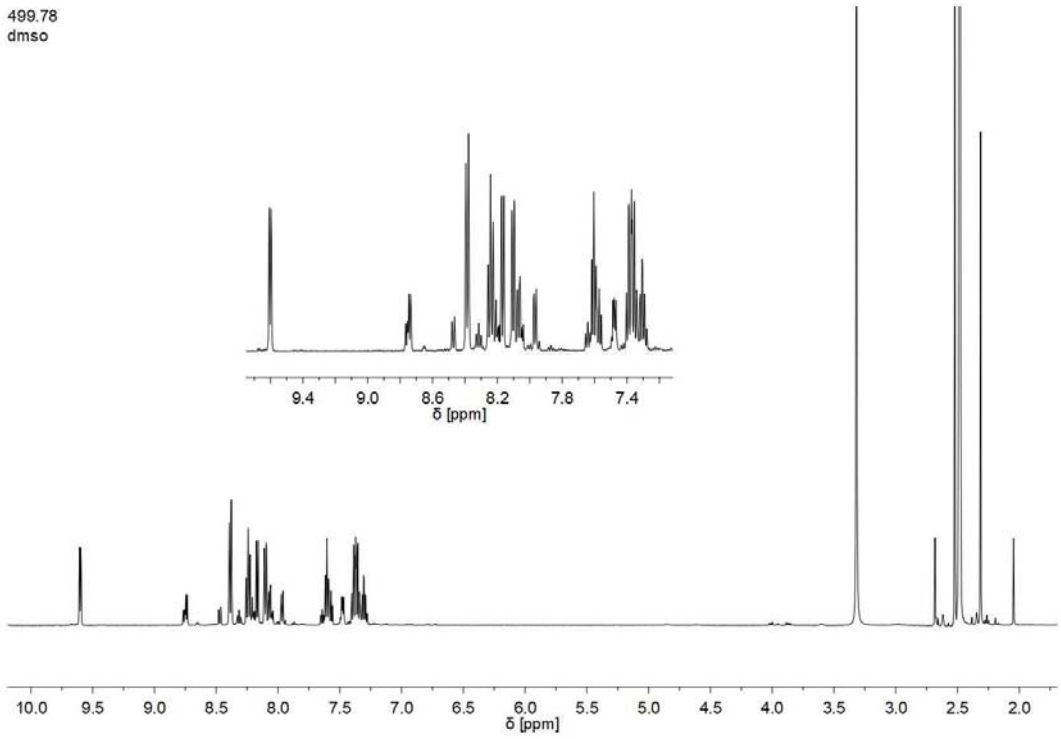

Figure S33. ^{1}H NMR spectra of **Ru1**.

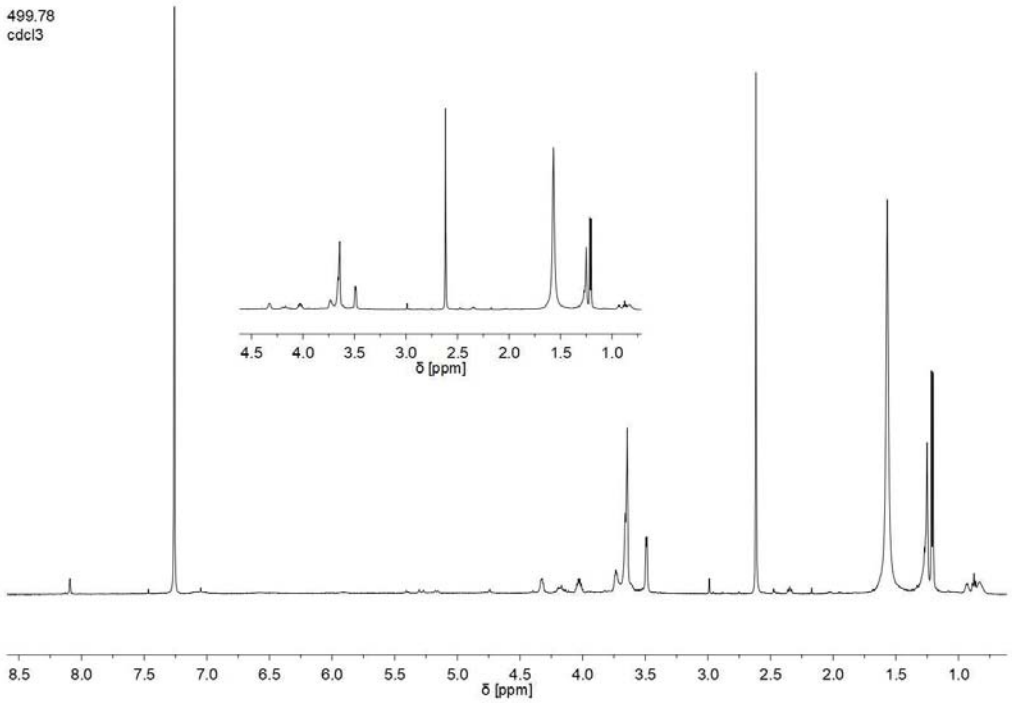

Figure S34. ^{1}H NMR spectra of allyl alcohol oligomer.

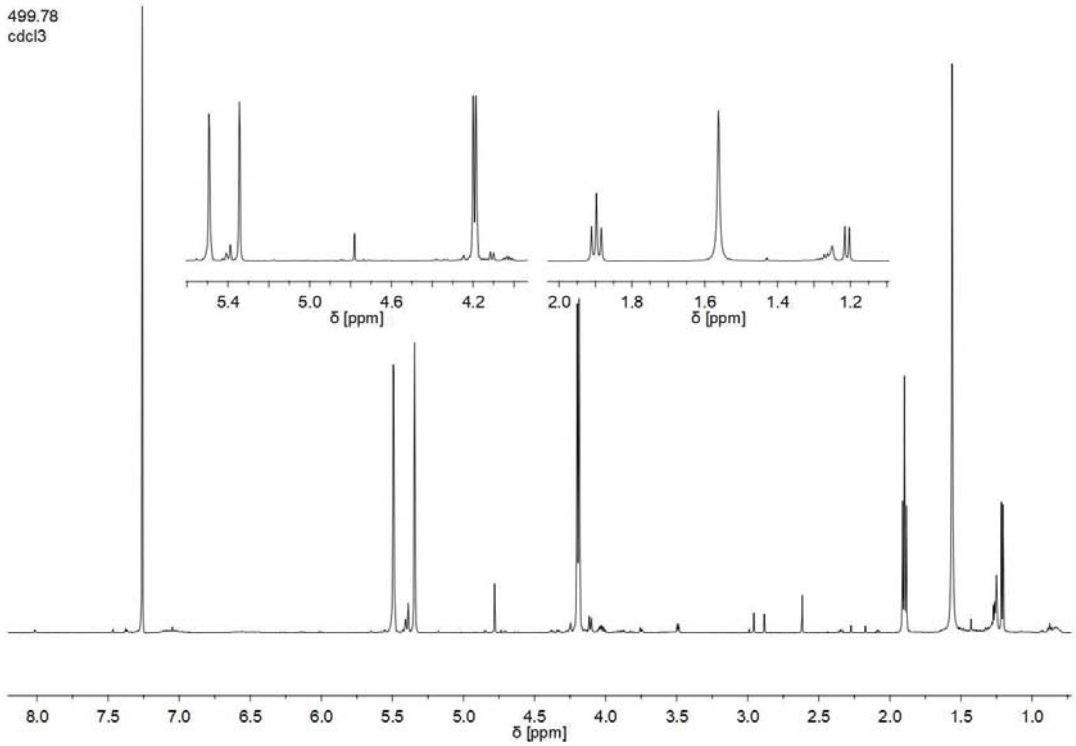

Figure S35 ^{1}H NMR spectra of 2-chloro-2-propen-1-ol oligomer.

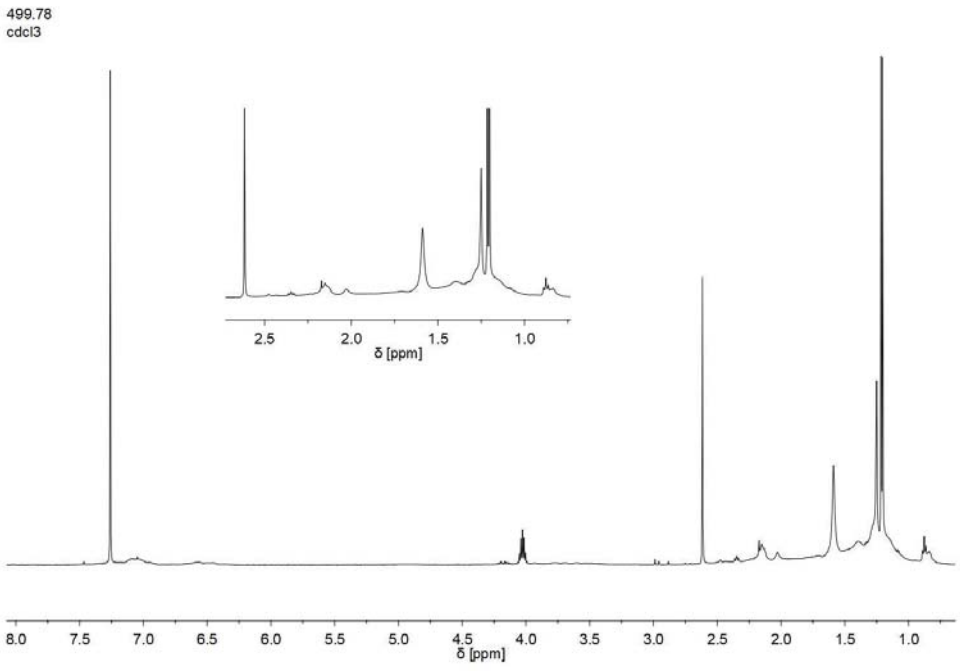

Figure S36. ^{1}H NMR spectra of 3-buten-2-ol oligomer.

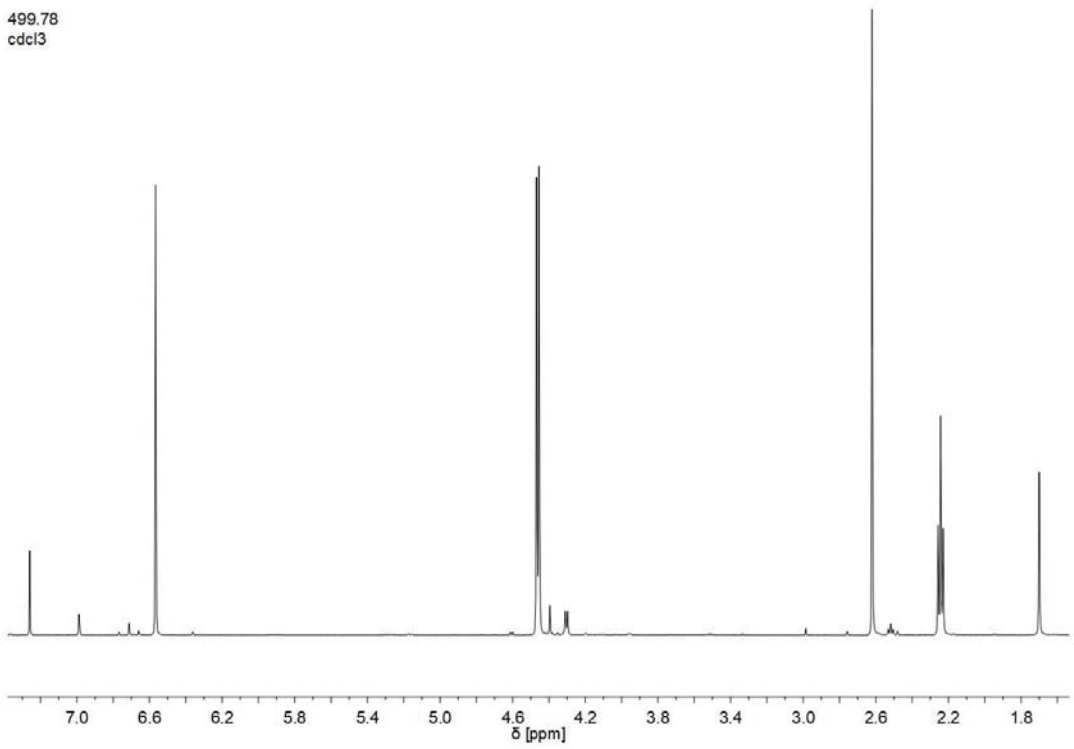

Figure S37. ^{1}H NMR spectra of 2,3-dibormo-2-propen-1-ol oligomer.

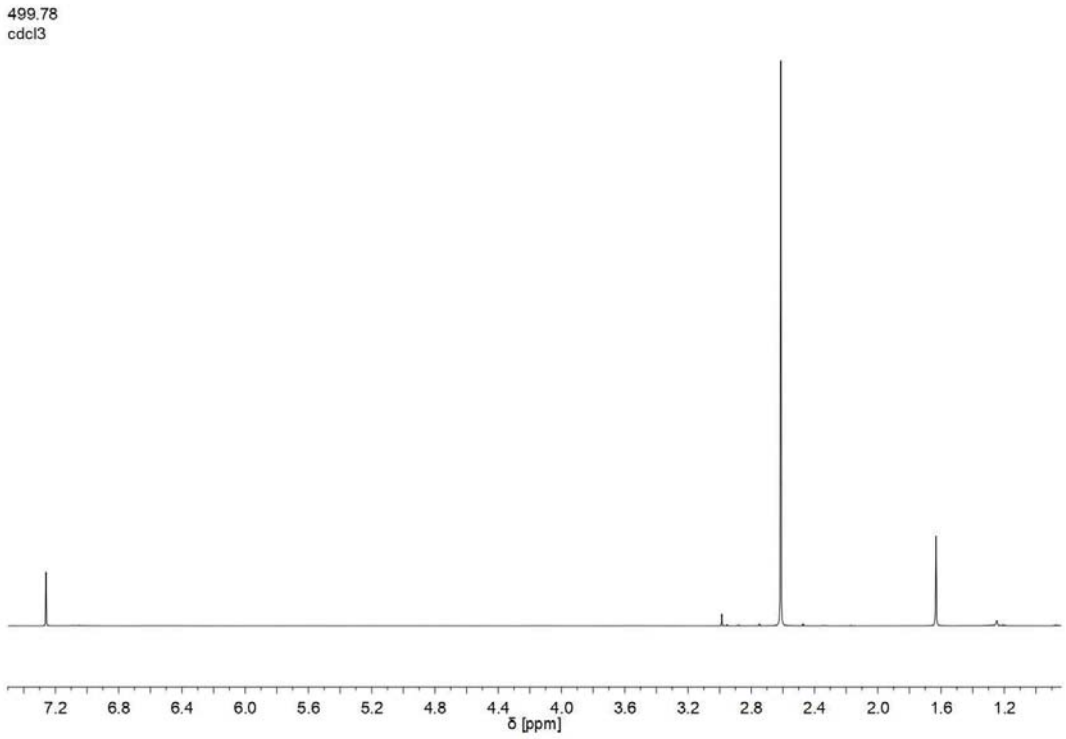

Figure S38. ^{1}H NMR spectra of ethylene oligomer.

References:

1 G. M. Sheldrick, *Acta Crystallogr C Struct Chem*, 2015, **71**, 3–8.
2 V. Petříček, M. Dušek and L. Palatinus, *Z Kristallogr Cryst Mater*, 2014, **229**, 345–352.
3 F. H. Allen, *Acta Crystallogr B*, 2002, **58**, 380–388.
4 C. R. Groom, I. J. Bruno, M. P. Lightfoot and S. C. Ward, *Acta Crystallogr B Struct Sci Cryst Eng Mater*, 2016, **72**, 171–179.
5 M. E. Frisch, G. W. Trucks, H. B. Schlegel, G. E. Scuseria, M. A. Robb, J. R. Cheeseman and D. J. Fox, .
6 P. J. Hay and Thom. H. Dunning, *J Chem Phys*, 1977, **67**, 2290–2303.
7 P. J. Hay and W. R. Wadt, *J Chem Phys*, 1985, **82**, 299–310.
8 J. P. Perdew, *Phys Rev B*, 1986, **33**, 8822–8824.
9 A. D. Becke, *Phys Rev A (Coll Park)*, 1988, **38**, 3098–3100.
10 C. Lee, W. Yang and R. G. Parr, *Phys Rev B*, 1988, **37**, 785–789.
11 S. Grimme, *J Comput Chem*, 2004, **25**, 1463–1473.
12 S. Grimme, *J Comput Chem*, 2006, **27**, 1787–1799.
13 S. Grimme, J. Antony, S. Ehrlich and H. Krieg, *J Chem Phys*, , DOI:10.1063/1.3382344.
14 S. Grimme, S. Ehrlich and L. Goerigk, *J Comput Chem*, 2011, **32**, 1456–1465.
15 S. F. Boys and F. Bernardi, *Mol Phys*, 1970, **19**, 553–566.
16 S. Simon, M. Duran and J. J. Dannenberg, *J Chem Phys*, 1996, **105**, 11024–11031.
17 R. Kamiński, K. N. Jarzembska and S. Domagała, *J Appl Crystallogr*, 2013, **46**, 540–543.
18 Y. Chen, K. N. Jarzembska, E. Trzop, L. Zhang and P. Coppens, *Chemistry – A European Journal*, 2015, **21**, 11538–11544.
19 D. Schaniel, N. Casaretto, E.-E. Bendeif, T. Woike, A. K. E. Gallien, P. Klüfers, S. E. Kutniewska, R. Kamiński, G. Bouchez, K. Boukheddaden and S. Pillet, *CrystEngComm*, 2019, **21**, 5804–5810.
20 A. A. Mikhailov, G. A. Kostin and D. Schaniel, *New Journal of Chemistry*, 2022, **46**, 12641–12650.
21 K. Nomura, W. Sidokmai and Y. Imanishi, *Bull Chem Soc Jpn*, 2000, **73**, 599–605.
22 T. Friedberger, J. W. Ziller and Z. Guan, *Organometallics*, 2014, **33**, 1913–1916.
23 M. A. Camacho-Fernandez, M. Yen, J. W. Ziller and Z. Guan, *Chem Sci*, 2013, **4**, 2902.
24 M. A. Camacho-Fernandez, J. W. Ziller and Z. Guan, *Organometallics*, 2022, **41**, 3257–3269.
25 P. COSSEE, *J Catal*, 1964, **3**, 80–88.
26 E. ARLMAN, *J Catal*, 1964, **3**, 99–104.
27 B. JAMES, *J Catal*, 1972, **27**, 442–451.
28 N. N. Dass and S. R. Sen, *Journal of Polymer Science: Polymer Chemistry Edition*, 1983, **21**, 3381–3388.
29 E. Zurek and T. Ziegler, *Prog Polym Sci*, 2004, **29**, 107–148.
30 K. P. Bryliakov, N. V Semikolenova, D. V Yudaev, V. A. Zakharov, H. H. Brintzinger, M. Ystenes, E. Rytter and E. P. Talsi, *J Organomet Chem*, 2003, **683**, 92–102.